

Major Research Experience

- Developed high-throughput characterization systems
- Prediction of material physical properties using artificial neural networks

Research Experience---High-throughput characterization systems

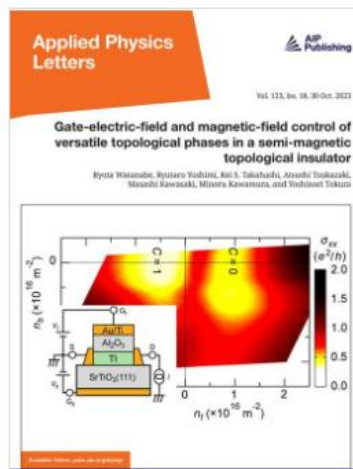
03/2022-06/2024 Shenzhen Large-scale Scientific Facility Platform Construction Project (Sub-project)

Major Achievements:

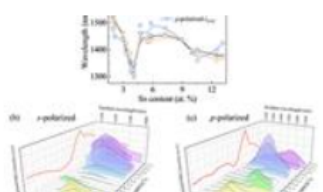
[System Design & Construction]

- Designed and built high-throughput time-domain micro-scale Magneto-Optic Kerr Effect (MOKE) characterization system (Temperature control: 1.7–300 K, Magnetic field: ± 7 T, Spatial resolution: 36.42 μm , Time resolution: fs-level).
- **Validated by Shenzhen Development and Reform Commission.**
- Designed and built high-throughput second-harmonic generation (SHG) characterization system (210 nm – 2100 nm Polarization-resolved)

[Demonstration Case: Study on Ultrafast Light–Matter Interaction Mechanism]



PHONONIC, ACOUSTIC, AND THERMAL PROPERTIES



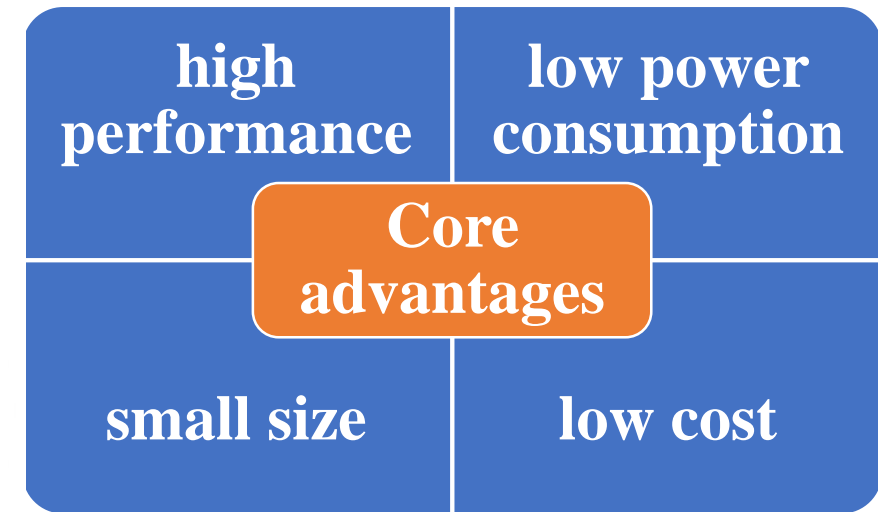
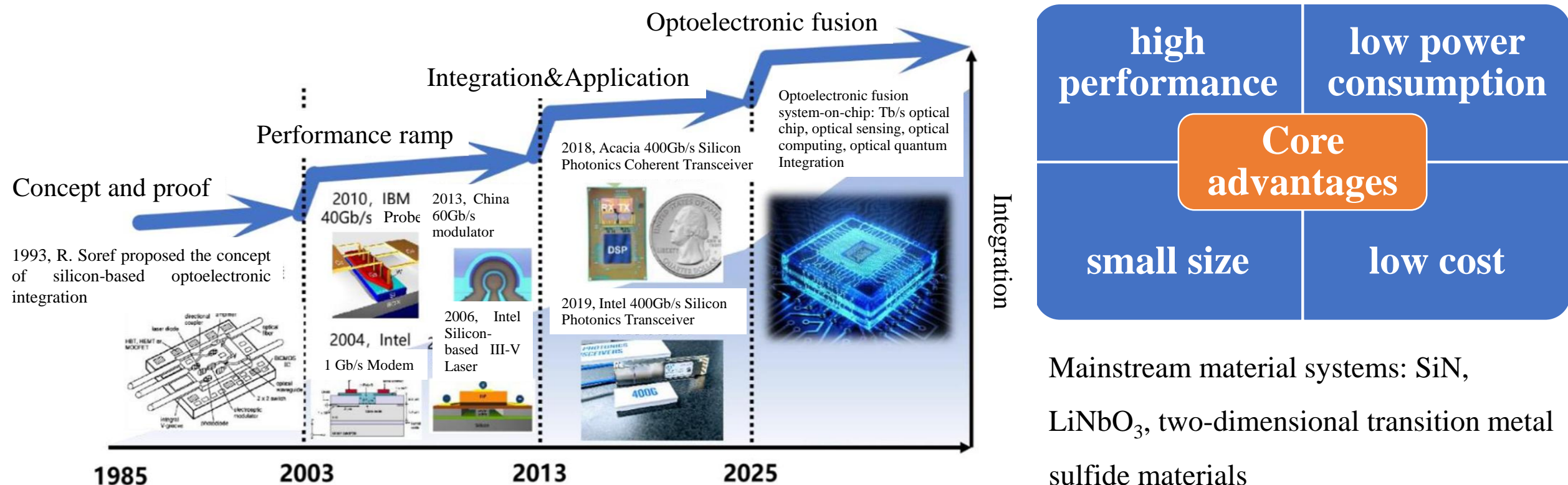
High-throughput investigation of second harmonic generation enhancement in indium tin oxide films: Effects of Sn doping

Xumin Wei; Chuanchuan Gu; X.-D. Xiang

Appl. Phys. Lett. 123, 182201 (2023) <https://doi.org/10.1063/5.0171095>

1 Introduction & Bottleneck

Optoelectronic Integration Techniques: One of the core technologies in the Post-Moore's Law Era.
The synergistic combination of mature microelectronics and broadband optoelectronics techniques.



Mainstream material systems: SiN, LiNbO₃, two-dimensional transition metal sulfide materials

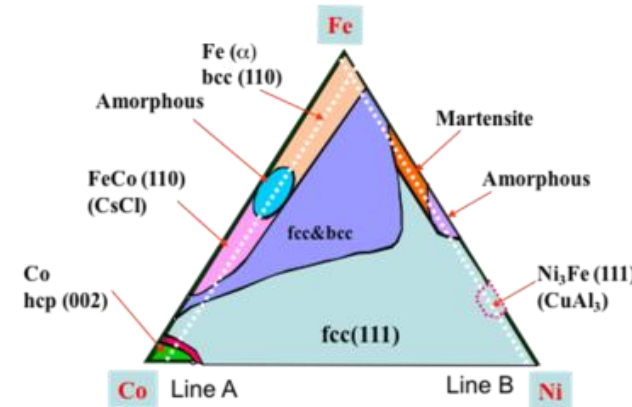
Bottleneck:

How can we accelerate the development of new materials and the exploration of novel physical principles?



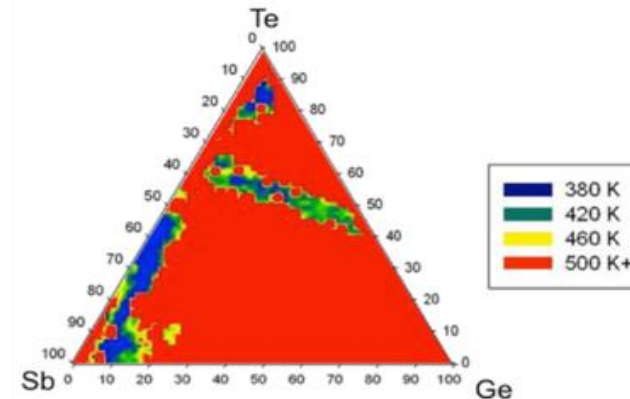
Composite material chip

X.-D. Xiang et al,
Science, 268, 1738(1995).



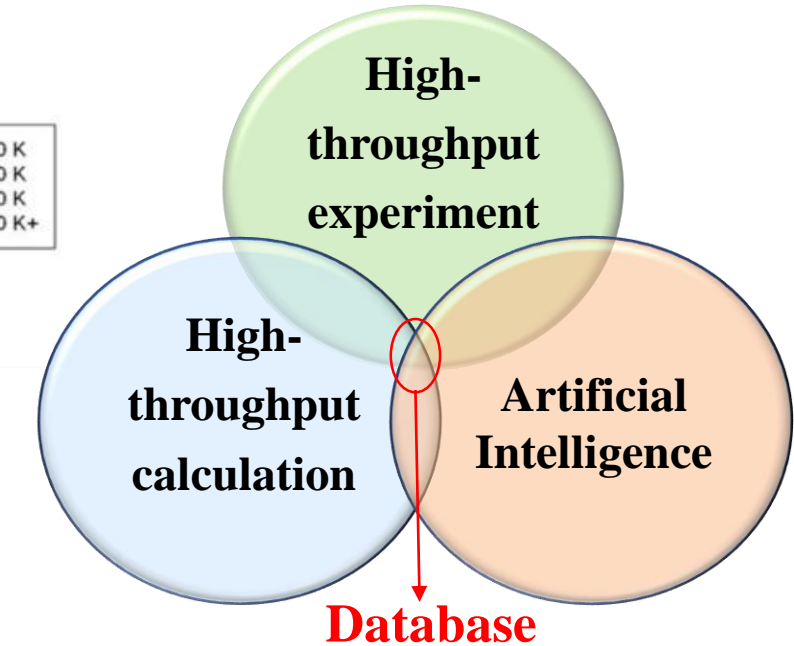
Parallel temperature rise & off-lattice characterization

X.-D. Xiang et al,
Intermetallics, 14, 241(2006).
Materials Gene Chip 1.0



In-situ synthesis & real-time characterization

X.-D. Xiang et al,
Engineering, 1, 225(2015).
Materials Gene Chip 2.0



High-throughput fabrication

High-throughput characterization

Quickly and accurately collect a large amount of experimental data

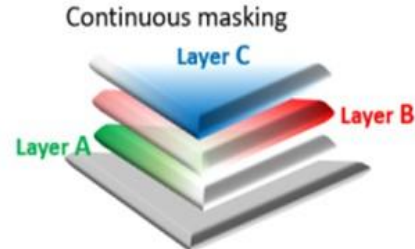
Enhance the efficiency of material optimization
Reduce the trial-and-error costs

Solution: Develop new high-throughput characterization techniques



1.2 High-throughput fabrication Techniques

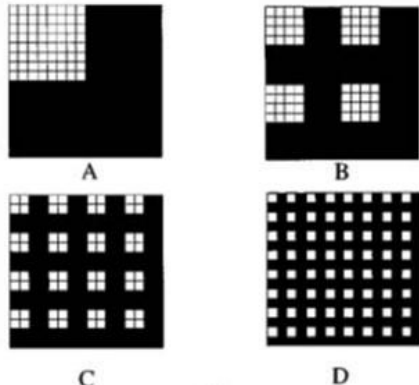
For multi-component thin film sample



Continuous Masking

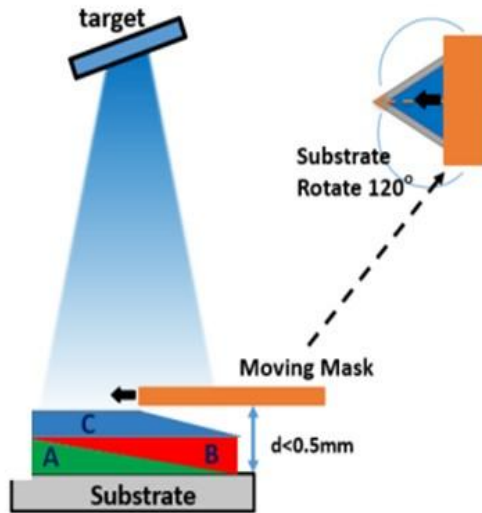
ACS Catalysis, 2022, 12(7): 3789-3796.

Splitting Masking

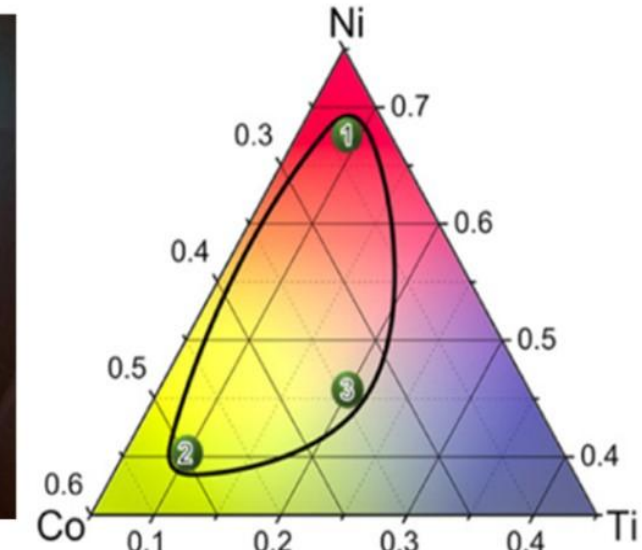


Fe Cr	Fe Y Cr	Fe Mg Mn	Fe Y Mn	W Mg Cr	W Y Cr	W Mg Mn	W Y Mn
Fe Mg	Fe Y	Fe Mg Ce	Fe Y Ce	W Mg	W Y	W Mg Ce	W Y Ce
Fe	Fe La Cr	Fe Mn	Fe La Mn	W Cr	W La Cr	W Ce	W La Ce
Mg Cr	Y Mn	Mg Mn	Y Mn	Ca Mg Cr	Ca Y Cr	Ca Mg Mn	Ca Y Mn
Cr	La Mn	La Mn	La Mn	Ca Cr	Ca Cr	Ca Mn	Ca La Mn
Mg	Y Ce	Mg Ce	Y Ce	Ca Mg	Ca Y	Ca Mg Ce	Ca Y Ce
La Ce	Ce	La Ce	La Ce	Ca La	Ca La	Ca Ce	Ca La Ce

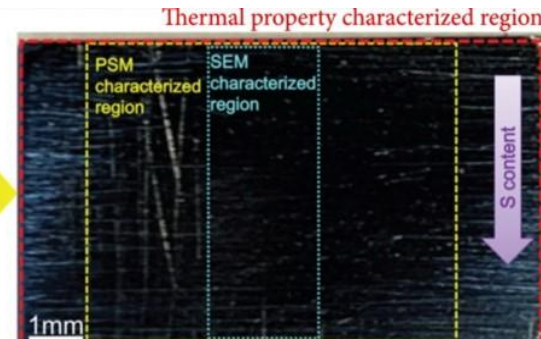
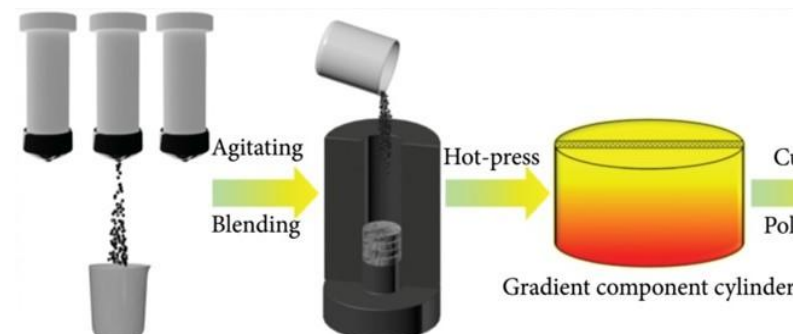
Science, 1998, 279: 1712-1714.



Co-sputtering deposition



High-throughput fabrication for bulk sample

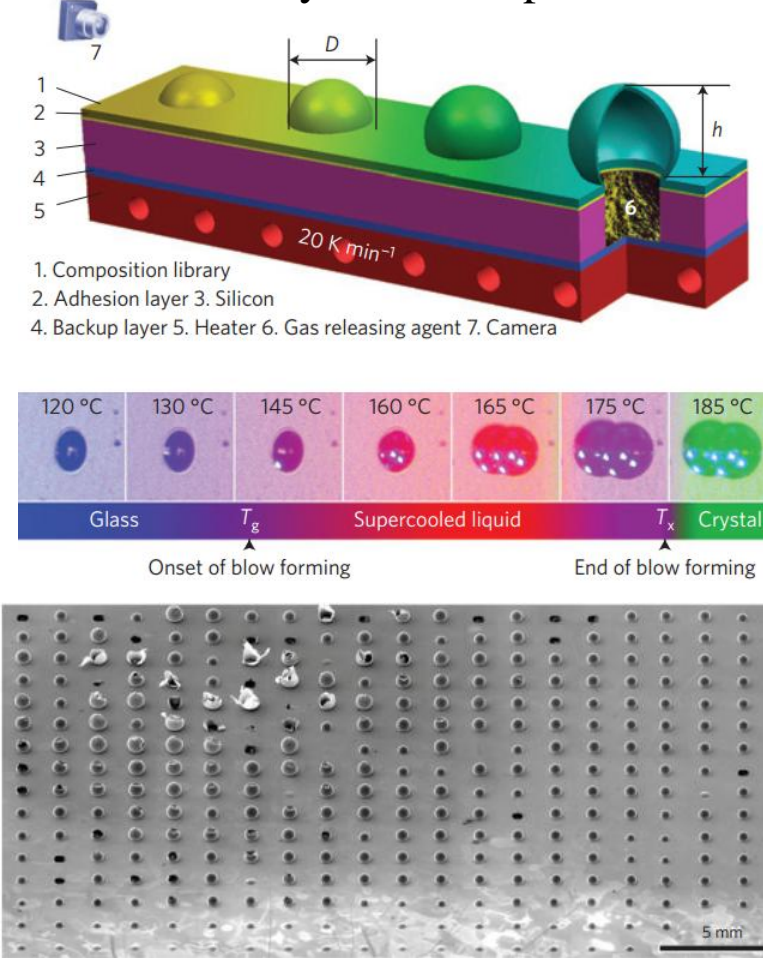


Energy & Environmental Science, 2019, 12(10): 3089-3098.



1.3 High-throughput characterization techniques

For the formability of thermoplastic materials

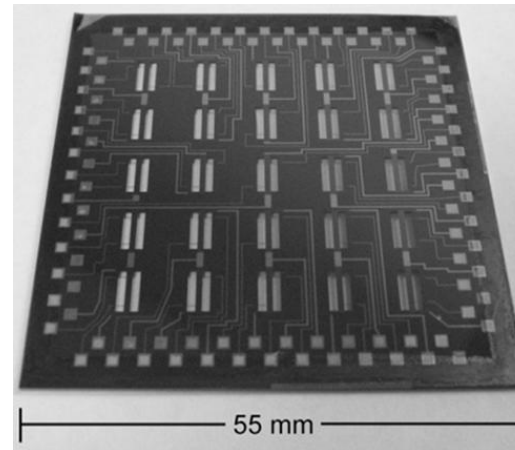


Nature Materials, 13(5), 494-500 (2014)

Challenge:

The characterization techniques for functional materials in integrated optoelectronics are still lacking.

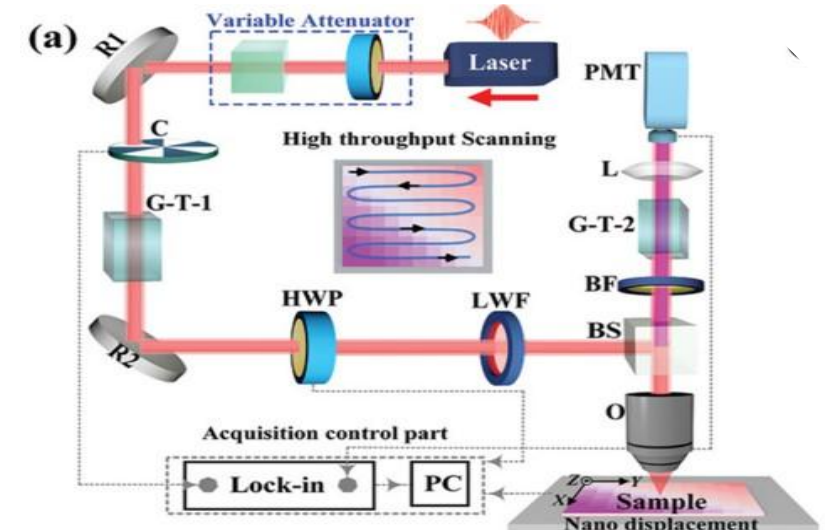
For thermodynamic parameters



Journal of Materials Research, 2010,
25(11): 2086-2100.

- Spatial resolution
- Signal-to-noise ratio
- Non-destructive
- Fast

For the nonlinear polarization rate of ferroelectric materials



Advanced Materials, 2023, 35(19): 2300348.

1.4 Contents

- Construction of a high-throughput characterization system for magnetic storage materials
- Construction of a high-throughput characterization system for high-speed signal transmission media & innovative Demonstration Case



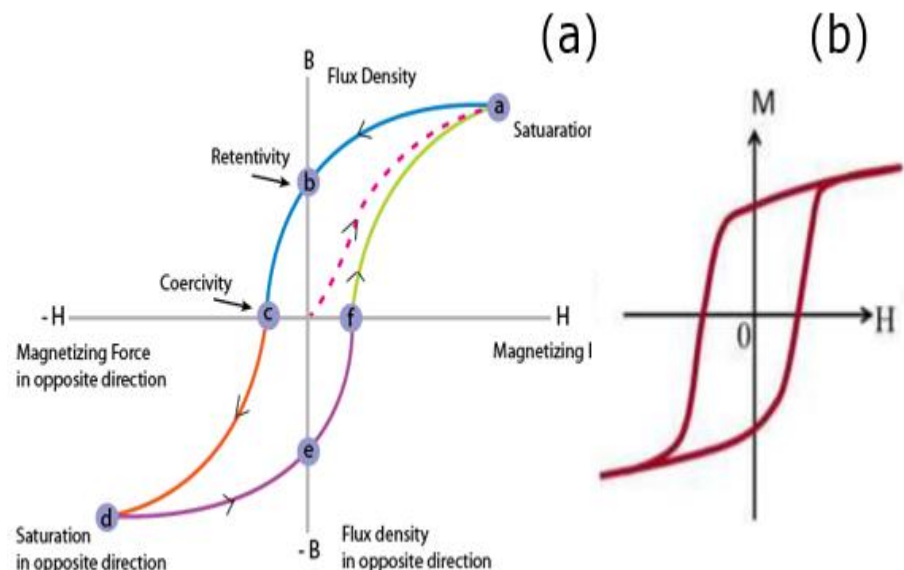
2 High-throughput characterization system for magnetic storage materials

Magnetic Storage Method: High-frequency external magnetic field rapidly rotates the magnetization direction, enabling the switching of circuit logic bit states.

Spin precession time is as fast as 2 ps.

Nature 428, 831–833 (2004).

Magnetic hysteresis loop



Superconducting Quantum Interference Device:
Measurement of single sample

Magnetic flux conversion to voltage

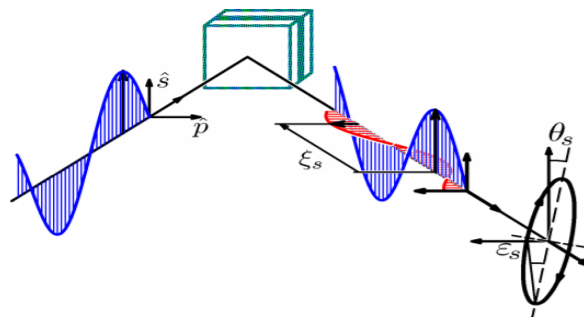
Traditional magnetic measurement technique is unable to achieve high-throughput and has low efficiency.



2.1 System Design Principles

System Function: Achieve high-throughput characterization of the multi-dimensional magnetic phase diagram of materials and ultrafast magnetization dynamics research at the ps scale.

Magneto-Optic effect



Different refractive indices → θ_{kerr}

Different absorption rates → η_{kerr}

The principles of measuring magnetic susceptibility using Magneto-Optic Kerr effect:

$$\theta_k = \frac{n^3 - n^2 \kappa^2 + 2n\kappa^2 - n}{(n^2 - \kappa^2 - 1)^2 + 4n^2 \kappa^2} Q \propto |\vec{M}| \cdot \lambda_L$$

In vacuum:

Kerr rotation angle θ_{kerr}
Kerr ellipticity η_{kerr}

$$\eta_k = \frac{n^2 \kappa - \kappa^3 - \kappa - 2n^2 \kappa}{(n^2 - \kappa^2 - 1)^2 + 4n^2 \kappa^2} Q \propto |\vec{M}| \cdot \lambda_L \quad \lambda_L: \text{Penetration Depth}$$

Magneto-Optic coefficient Q is proportional to the magnetization intensity

The magnetic susceptibility of materials: $\chi_K = \frac{\partial M}{\partial H} \propto \frac{\partial Q}{\partial H}$

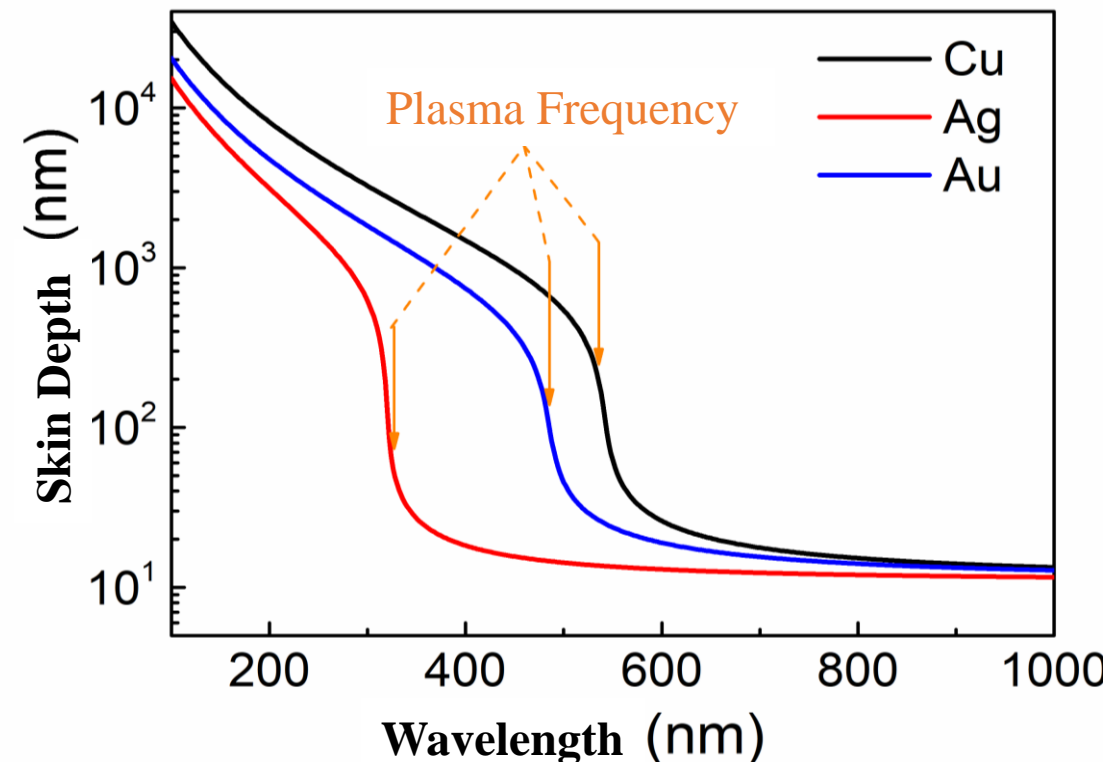


2.2 Technique Highlights

- Near the frequency of the material plasma, the penetration depth of the incident light into the material significantly increases, and the plasma resonance frequencies of different metal materials are different.
- Tunable ultraviolet-visible large source. Cover the plasma frequency range of most metal materials for high-throughput magneto-optical Kerr characterization.

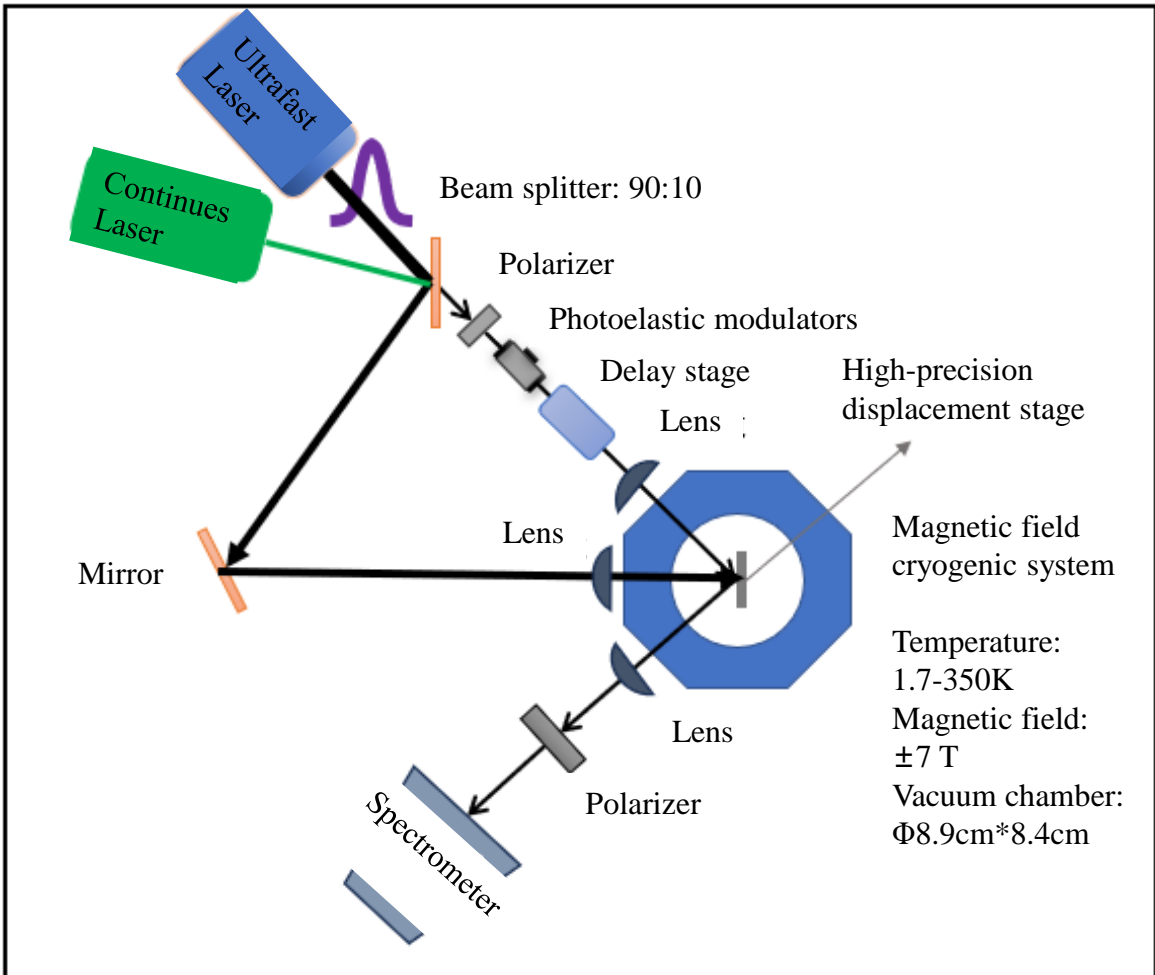
The metals' skin depth varies with the wavelength

Spectrometer





2.3 Optical Path Design



Measurement methods:

➤ **Small-angle method:** By measuring the Kerr rotation angle of the linearly polarized light reflected from the sample surface. The magnetism of the sample can be characterized.

When p-polarized laser incident, the intensity measured by the polarizer in front of the light detector:

$$I = |E_p \sin \delta + E_s \cos \delta|^2 \approx |E_p \delta + E_s|^2 \approx |E_p|^2 \delta^2 \left(1 + \frac{2\theta_k}{\delta}\right) \propto \theta_k$$

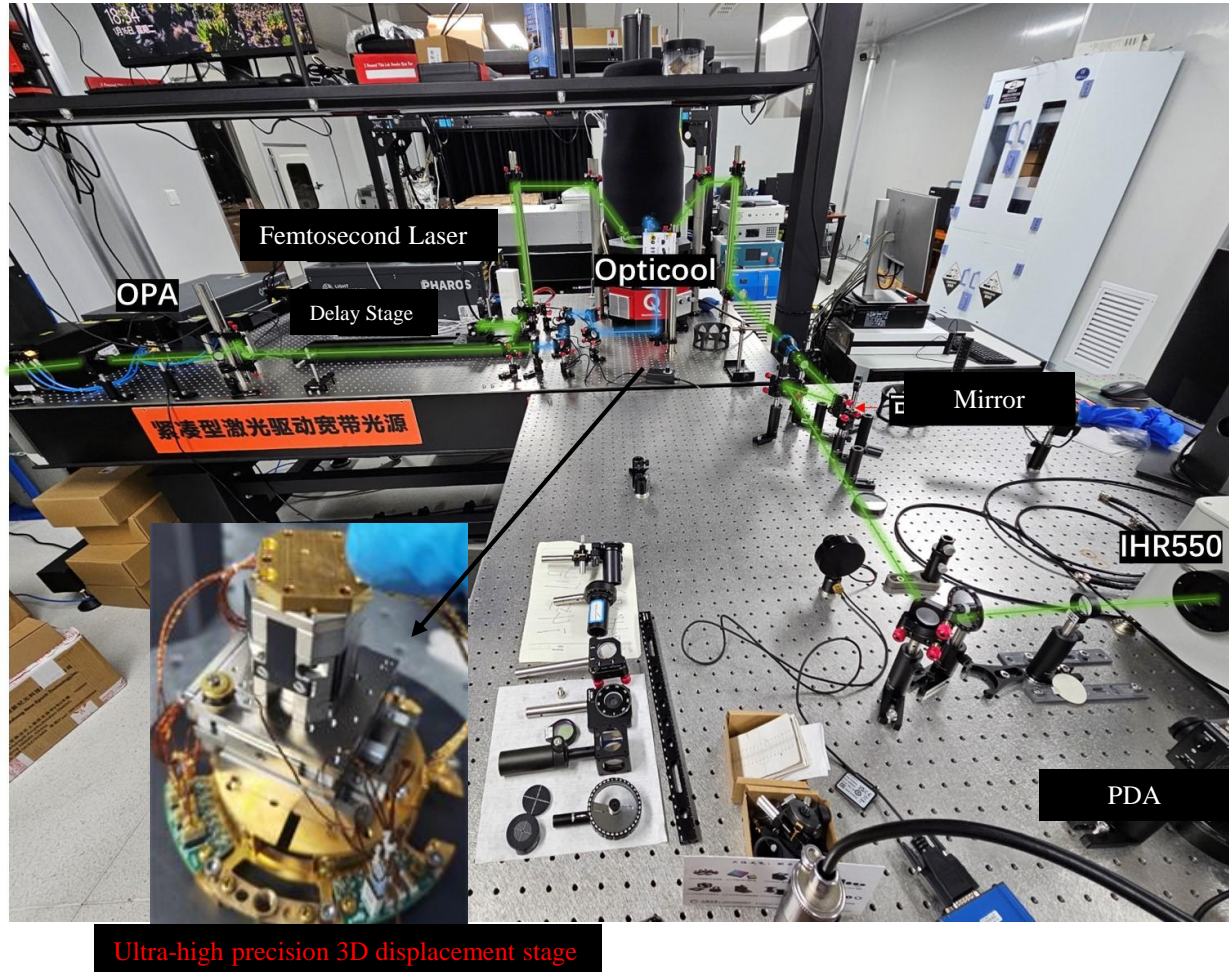
➤ **Magnetic circular dichroism method:** Using photoelastic modulators, a beam of linearly polarized light is converted into left-handed and right-handed circularly polarized light and irradiated onto the sample. Measure the difference in reflectance of the two circularly polarized lights under a magnetic field.

$$\theta_{RMCD} = \frac{R_{\text{right}} - R_{\text{left}}}{\bar{R}}$$



2.4 Optical Path Photo

key components:

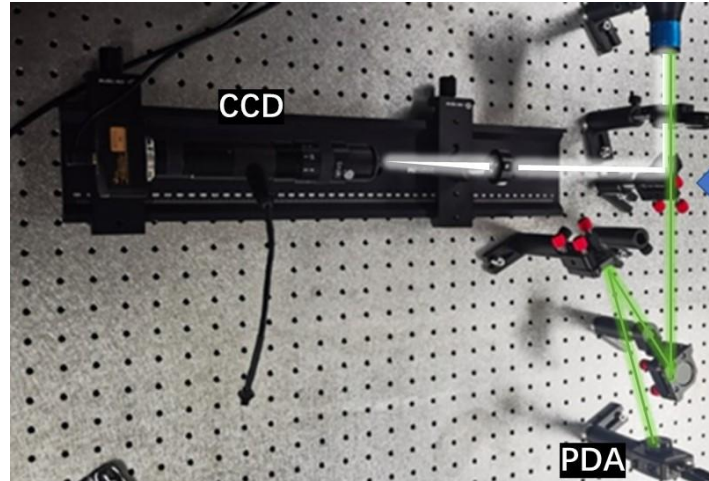
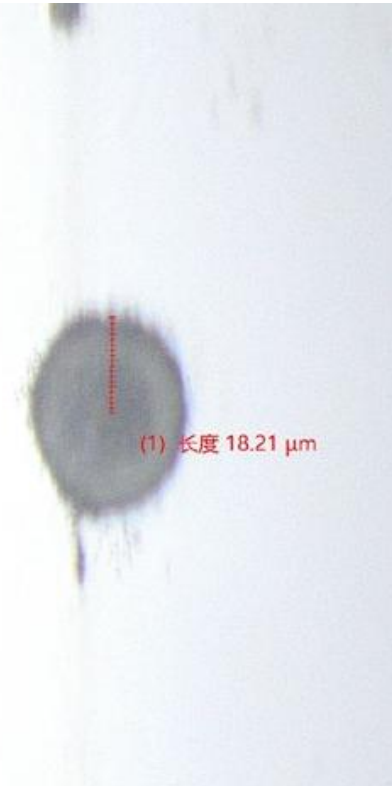


- **Magnetic field cryogenic system:** Integrates extreme conditions such as low temperature and strong magnetic fields to achieve intelligent temperature control and automatic field variation requirements. The temperature can be as low as 1.7 K, and the magnetic field can be as high as 7 T.

- **Ultra-high precision 3D displacement stage:** Constructs a three-degree-of-freedom nano-motion system that can achieve x, y, and z-axis motion, including two horizontal displacement stages and one vertical displacement stage. It can adapt to extreme conditions of extremely low temperatures (≤ 2 K) and strong magnetic fields (≥ 7 T).

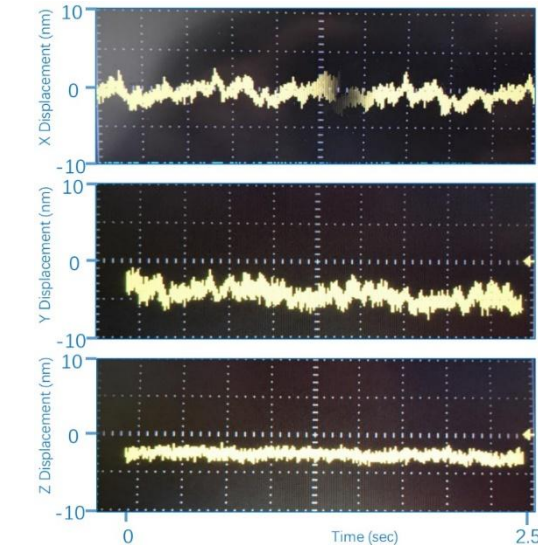
2.5 System Performance

✓ Spatial resolution: 36.42 micrometers



Spot size: diameter 36.42 μm

Imaging system resolution: better than 50 μm



Fine Positioning Mode
fine linear positioning range @ 300 K
fine linear positioning range @ 4 K
fine positioning resolution

5 μm
0.8 μm
sub-nm

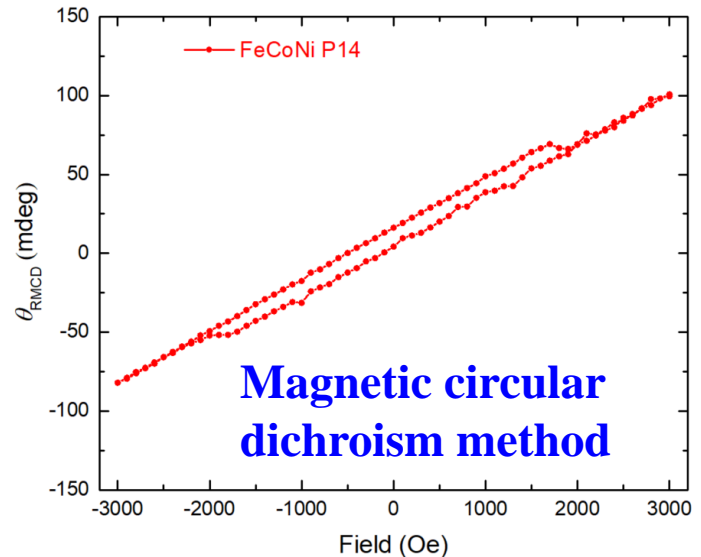
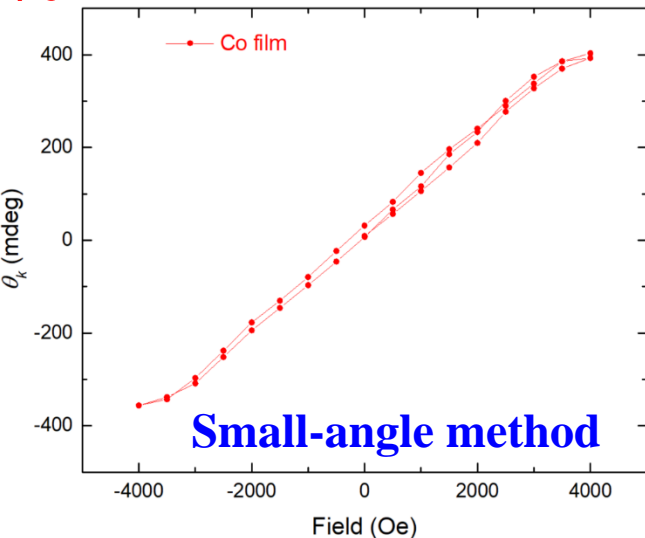
System stability better than 10 nm
Displacement stage accuracy up to sub-micron level

2.5 System Performance

✓ System measurement accuracy: 0.1%

➤ Small-angle method:

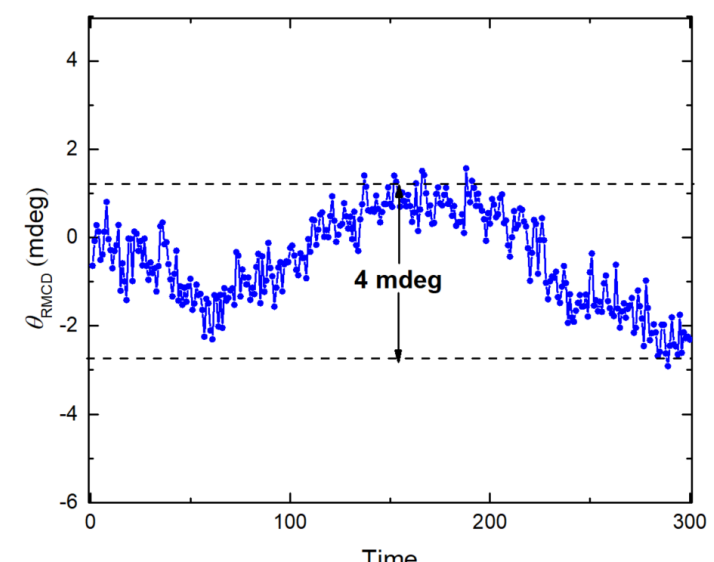
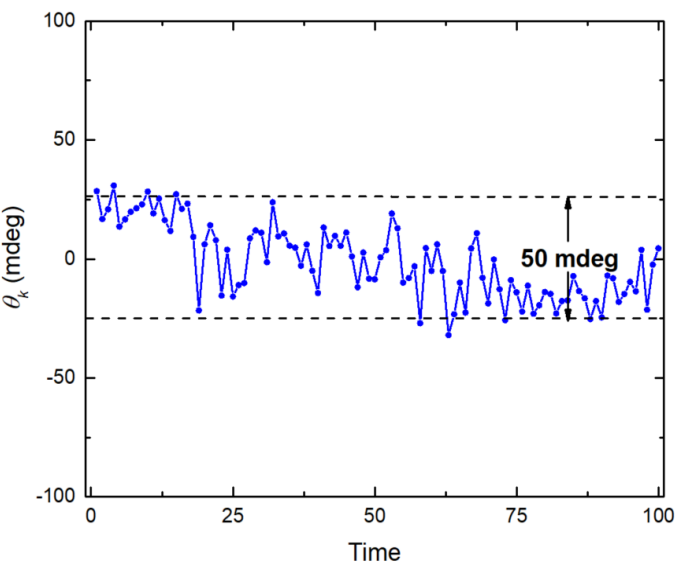
Data on the magnetic-optical Kerr angle of the Co film measured as a function of the magnetic field. Multiple measurement data with measurement accuracy ~ 50 mdeg, approximately 0.08%.



➤ Magnetic circular dichroism method:

The magnetic optical signal changes of the measured FeCoNi multicomponent thin film at point 14 with the magnetic field show obvious magnetic hysteresis behavior.

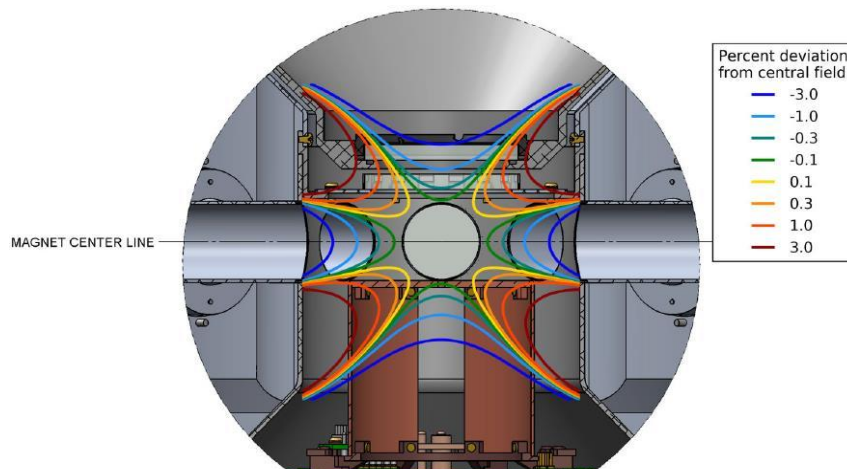
Multiple measurement data, with a measurement accuracy ~ 4 mdeg, approximately 0.007%.



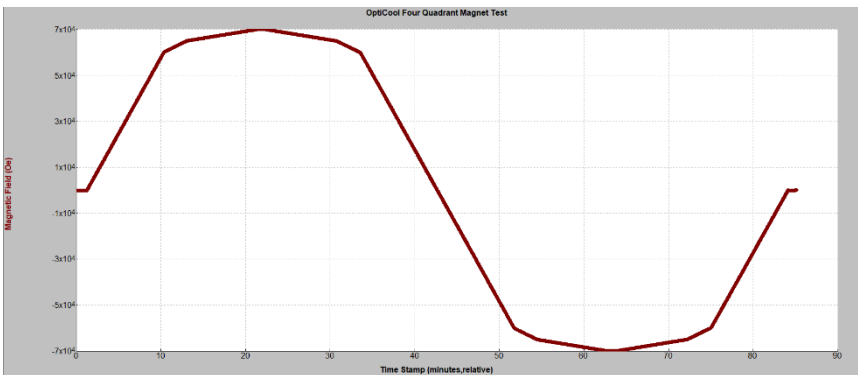


2.5 System Performance

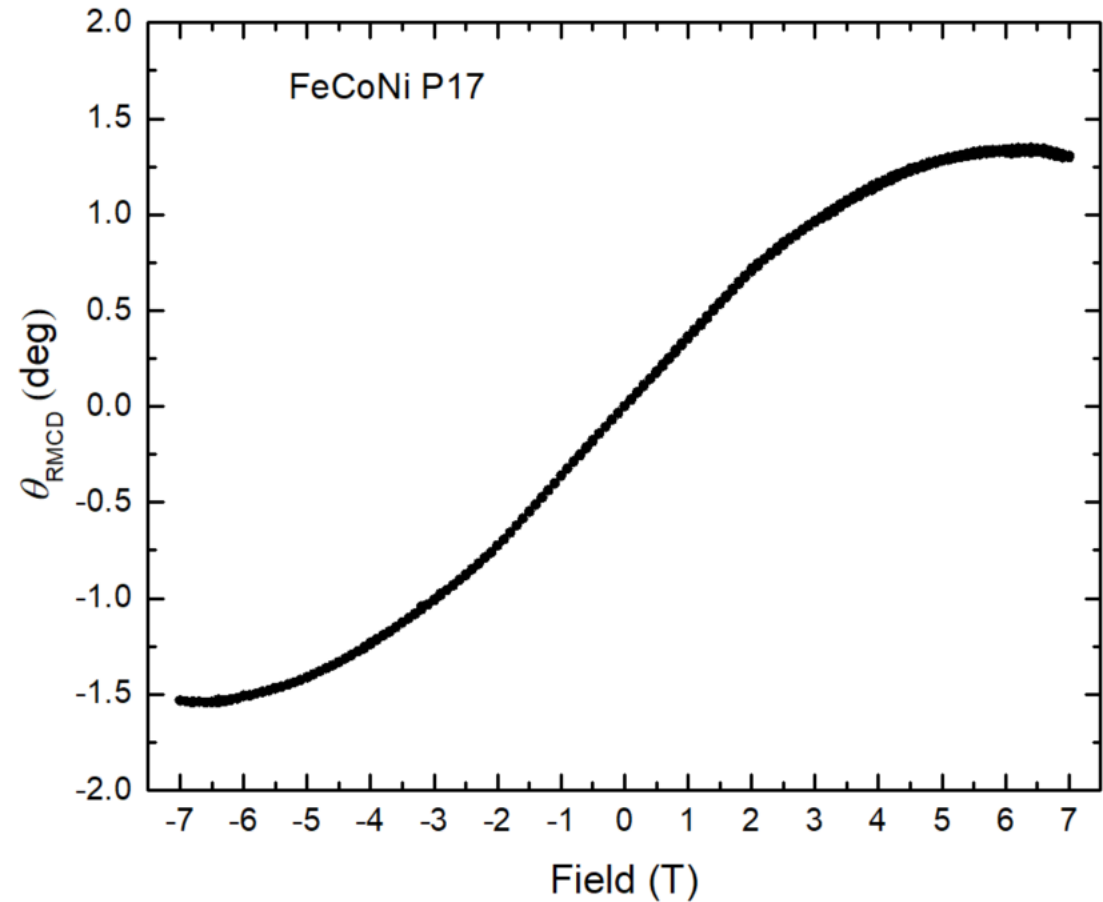
✓ System magnetic field: ± 7 T



Magnetic field uniformity: $\pm 0.3\%$ (3 centimeter ball)



The lower figure shows the magnetic field increased to 7 T.

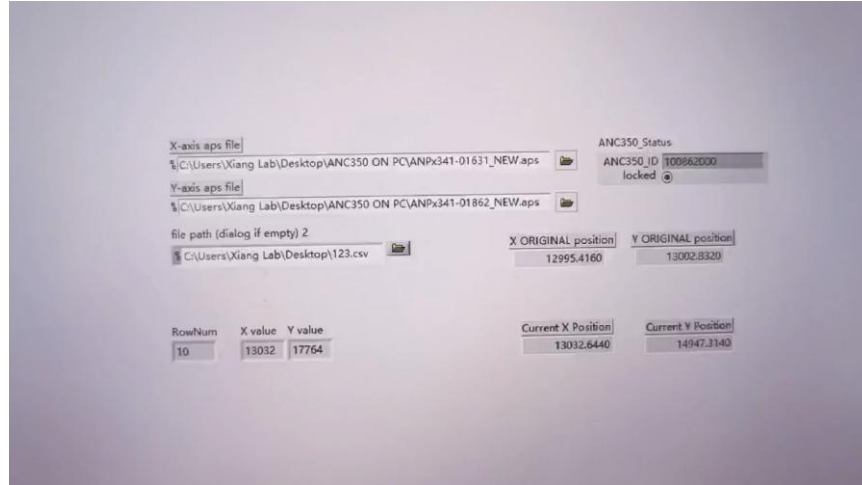


Measurement of magneto-optical effects of FeCoNi multicomponent thin films at point 17 to ± 7 T using magnetic circular dichroism method

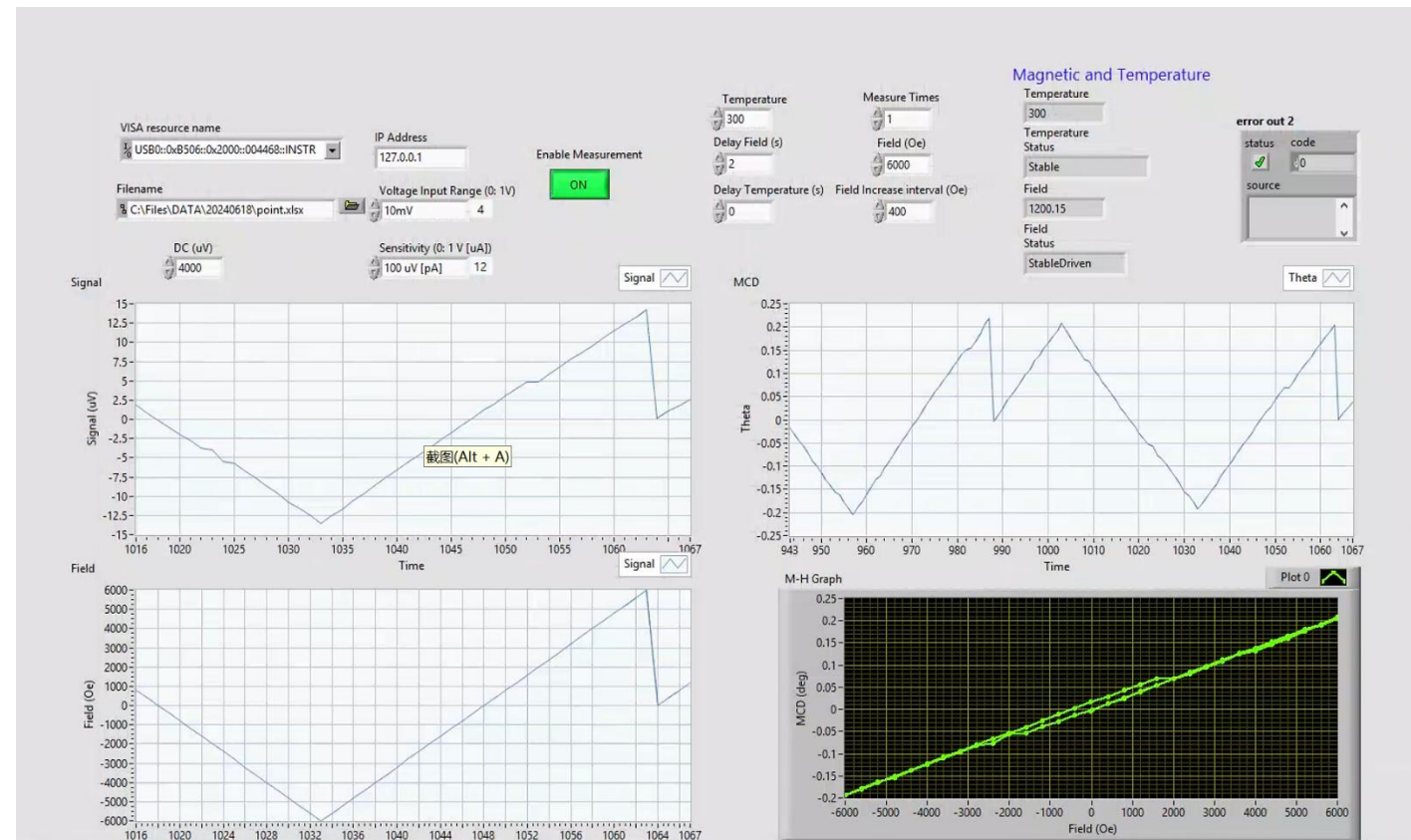


2.6 Automated measurement program

Displacement control



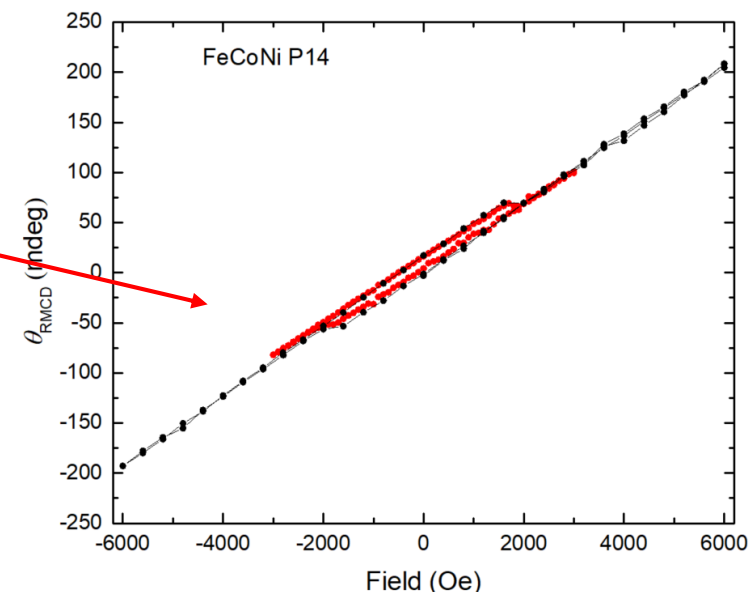
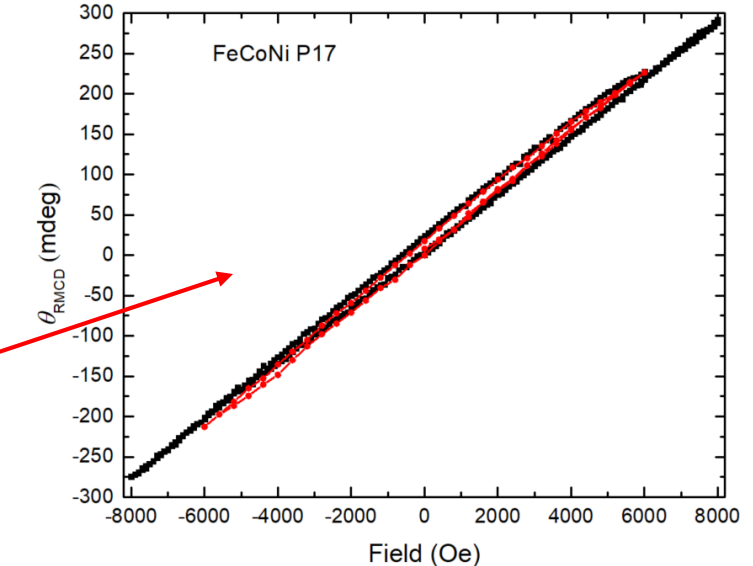
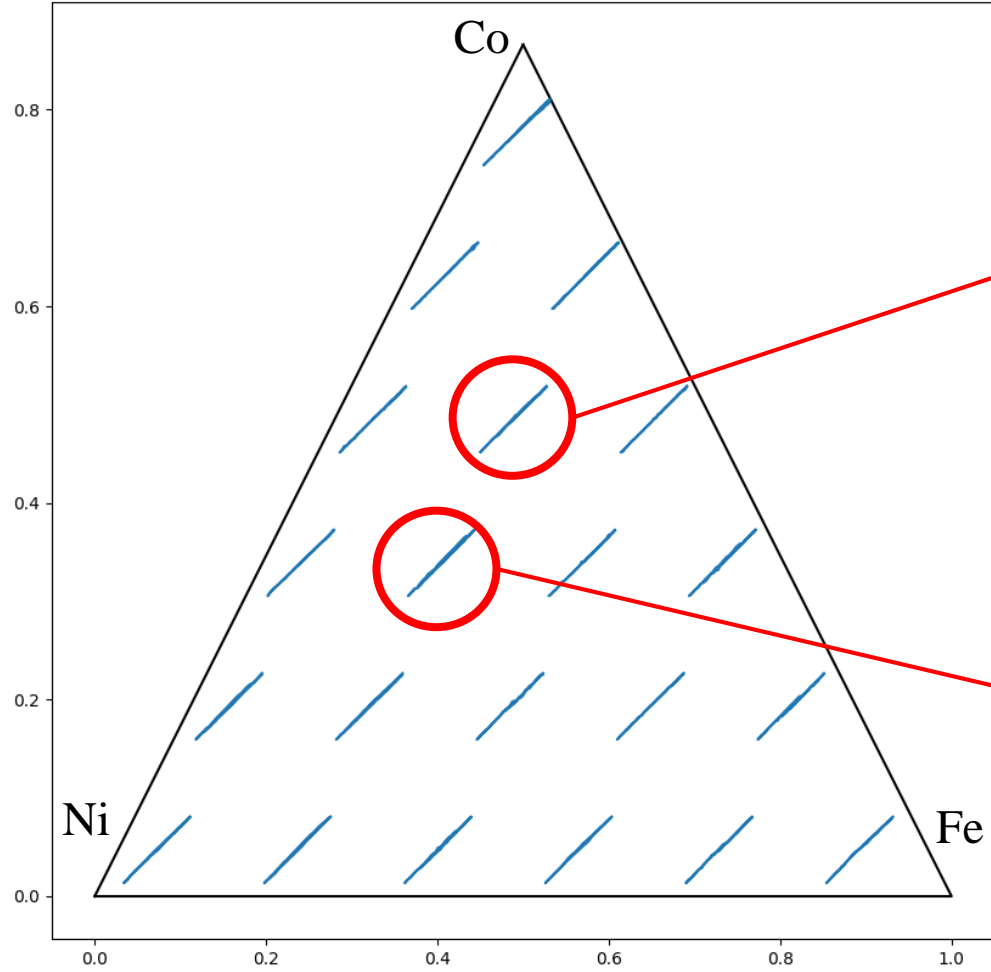
Data collection





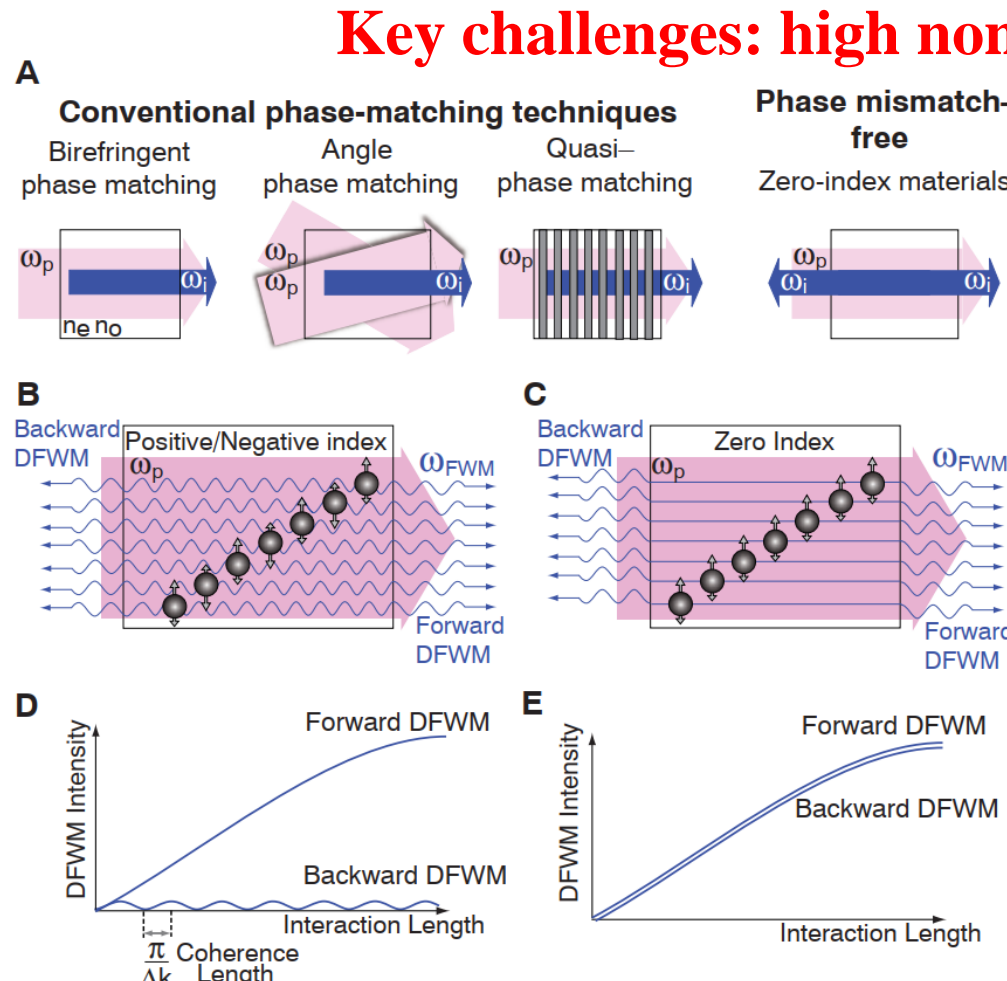
2.7 Case

FeCoNi Multi-component magnetic phase diagram

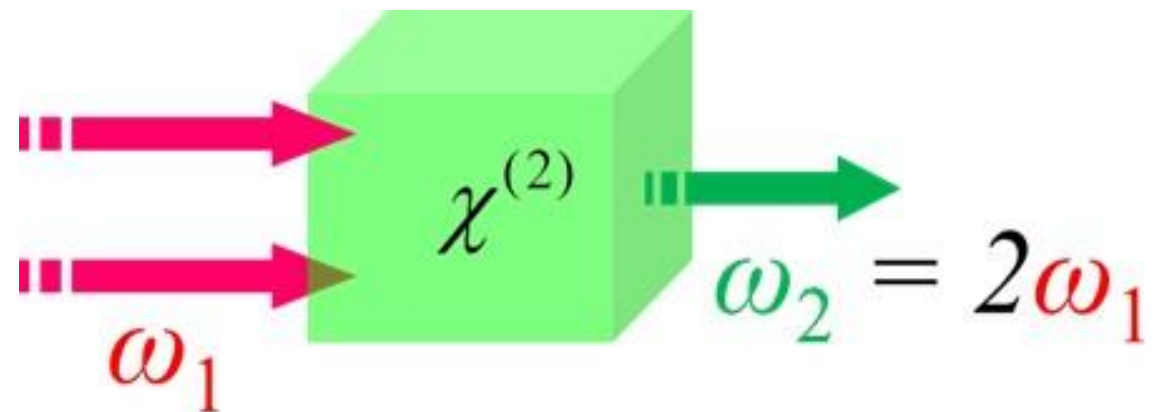


3 High-throughput characterization system for High-speed signal transmission media

Optical nonlinear materials are widely used in high-speed signal transmission media.



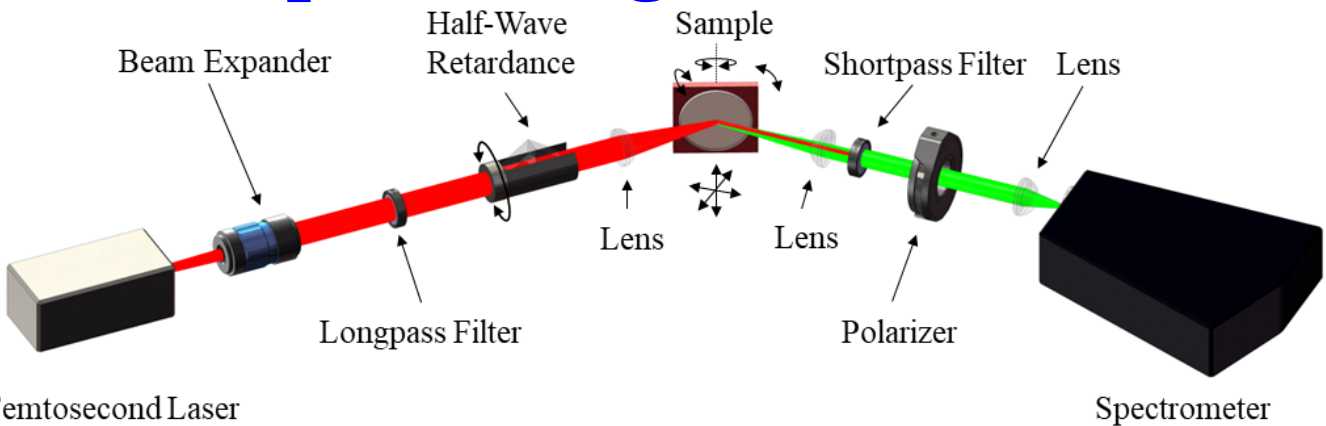
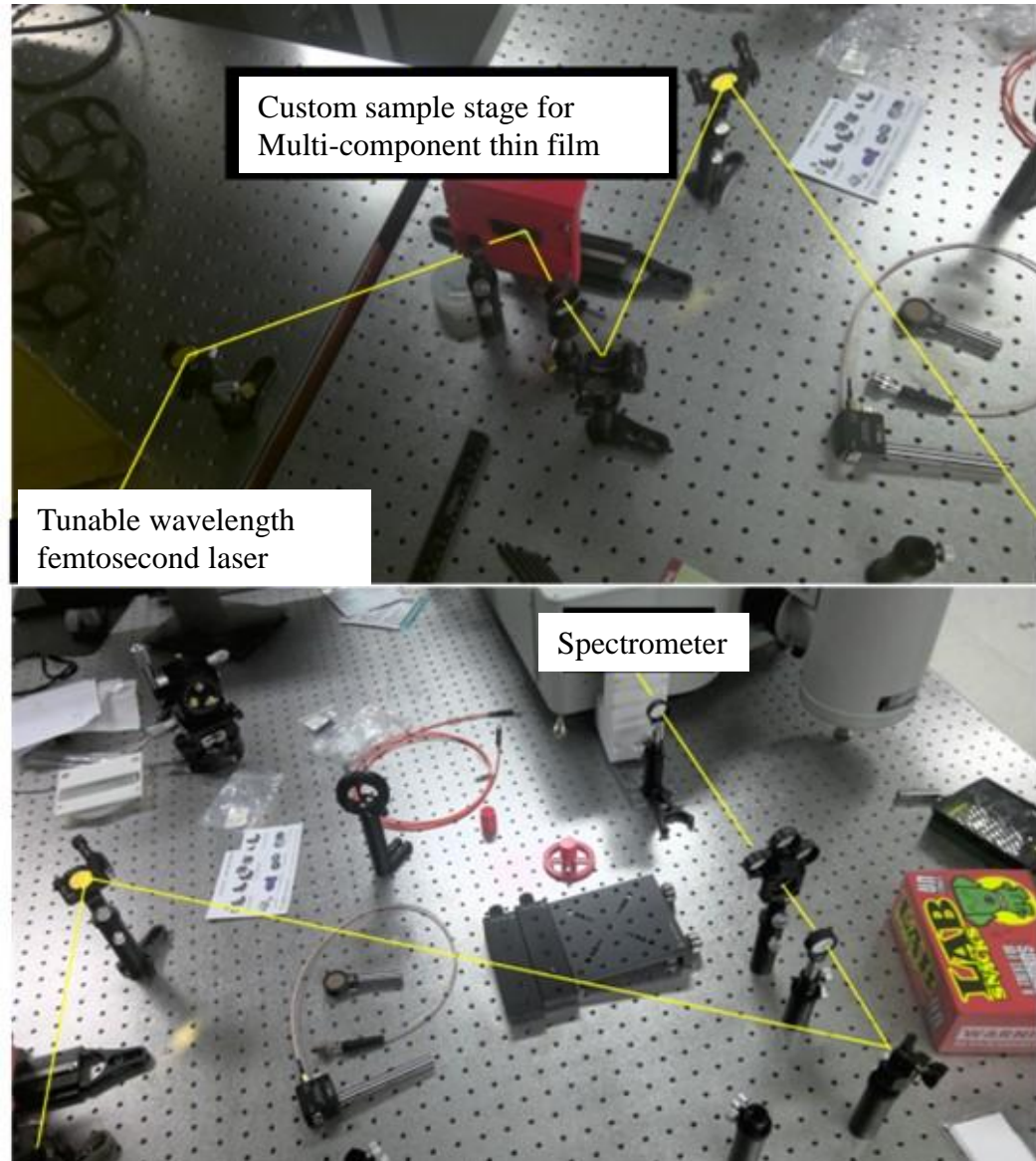
Principle:



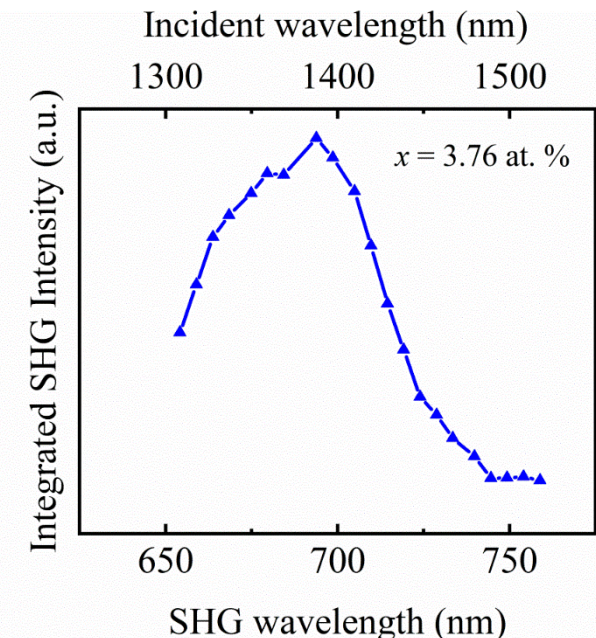
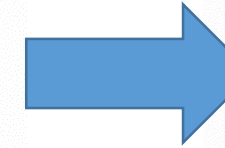
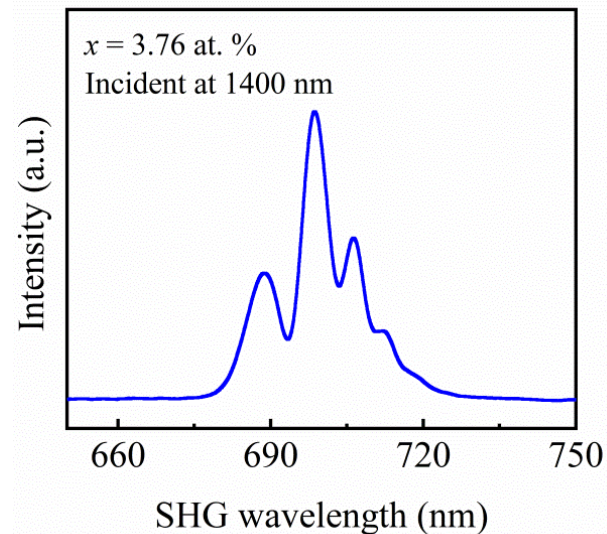
Second harmonic generation (SHG) measurement is a commonly used method for evaluating nonlinear response.



3.1 SHG reflection measurement optical path & data processing



Data processing:

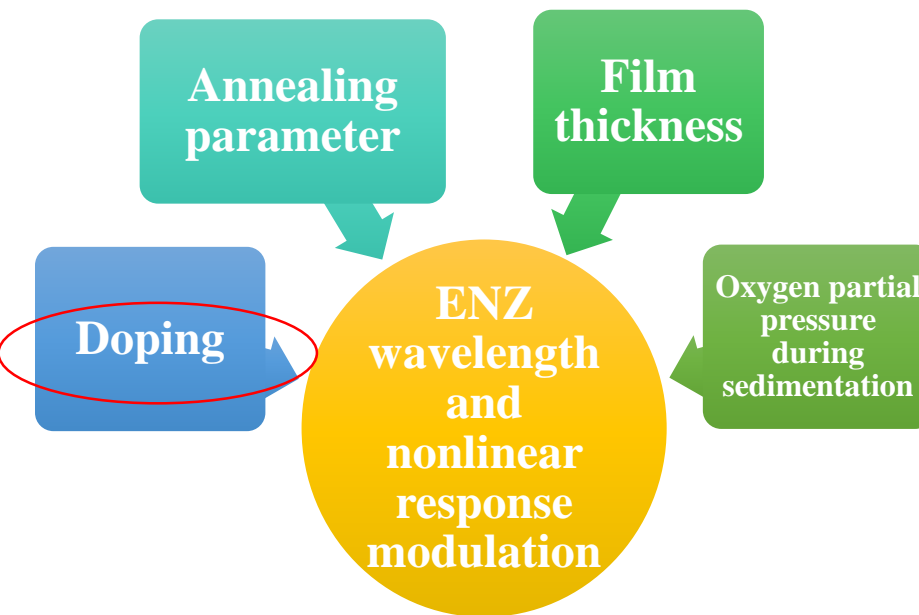
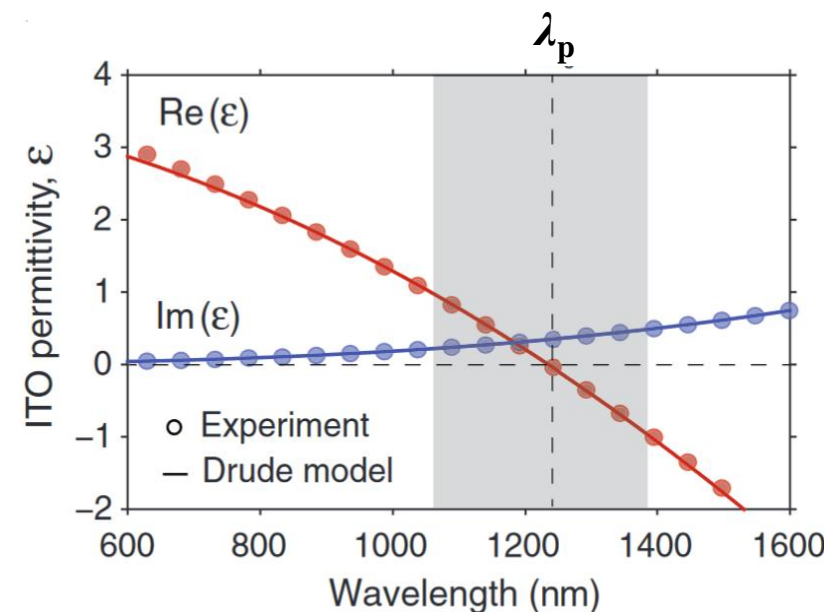


Integrated-SHG spectrum

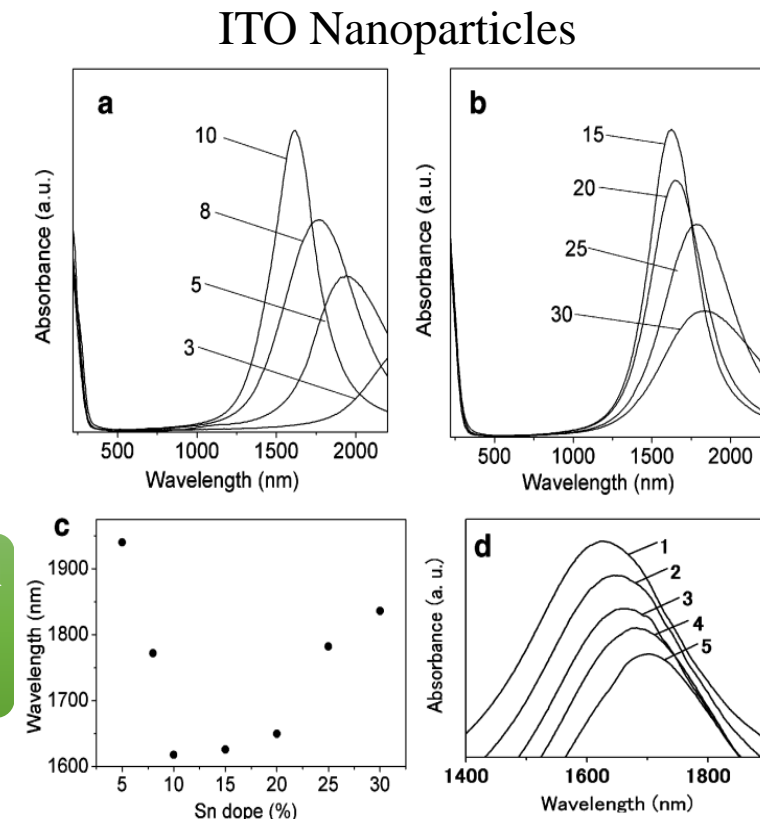
3.2 Low-loss transmission media - transparent conductive material ITO

Epsilon-Near-Zero (ENZ) materials:

- Dielectric constant is almost zero at ENZ wavelength. $n = \sqrt{\epsilon\mu} \sim 0$
- Near-zero refractive index, no phase matching required $|\epsilon| < 1$



Science 352(6287), 795–797 (2016).

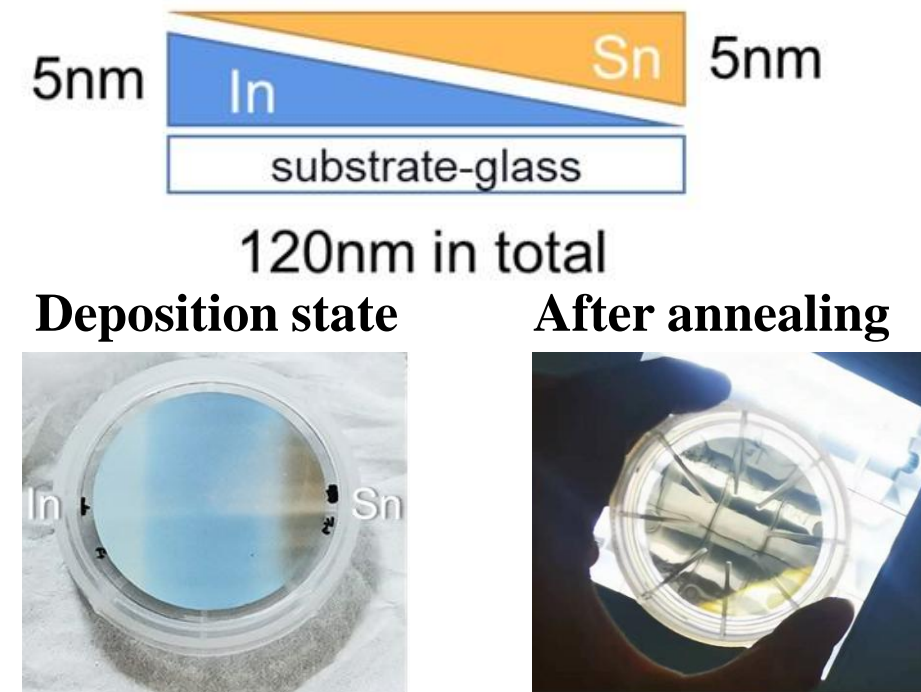
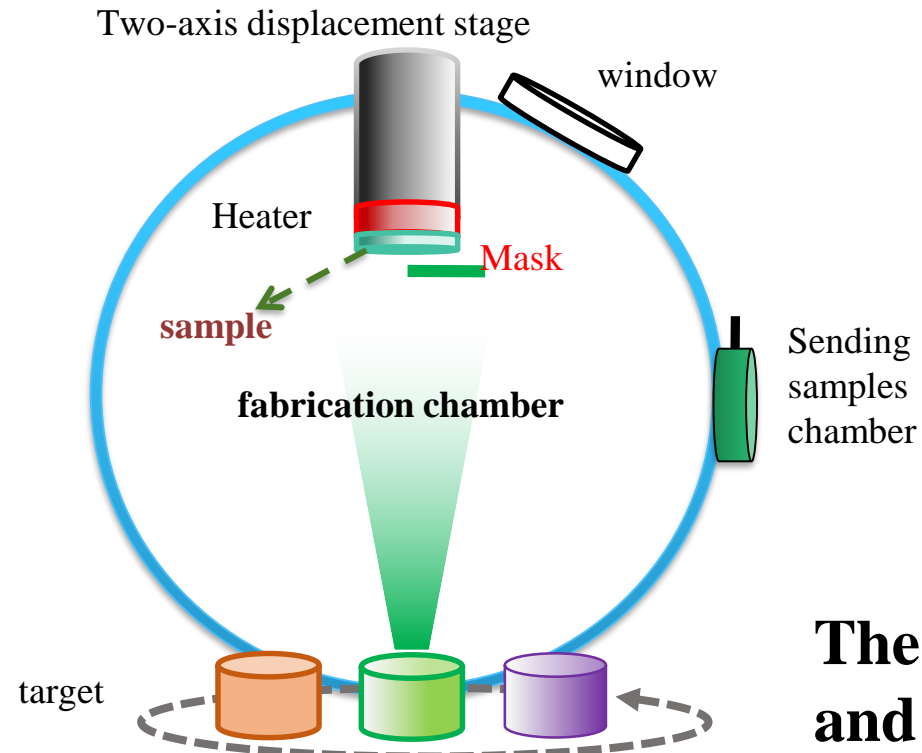
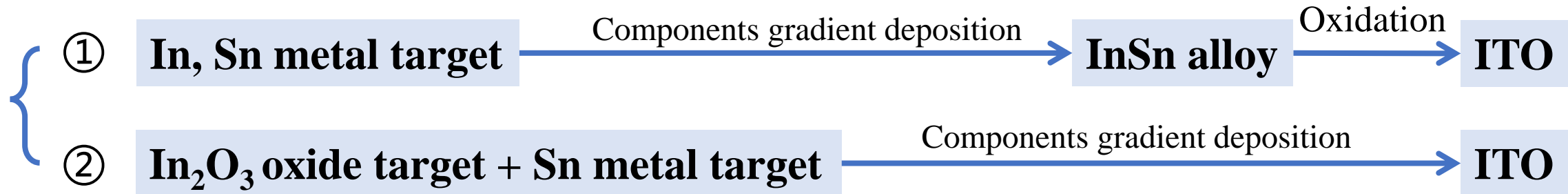


J. Am. Chem. Soc. 131 (49), 17736-17737 (2009)

Lack of systematic research on the optical nonlinearity effects of continuous Sn doping on ITO thin films.



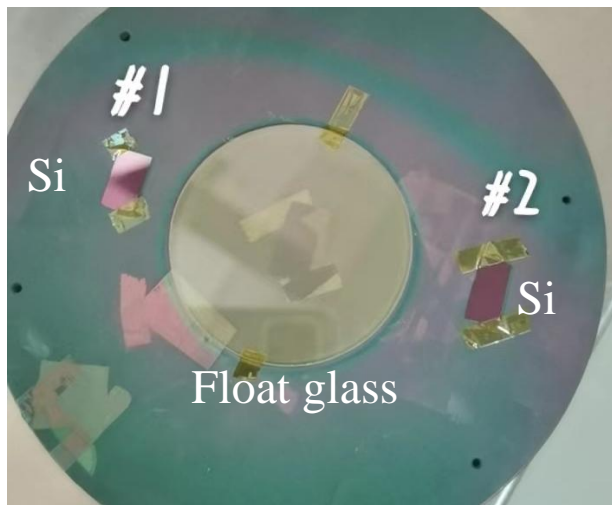
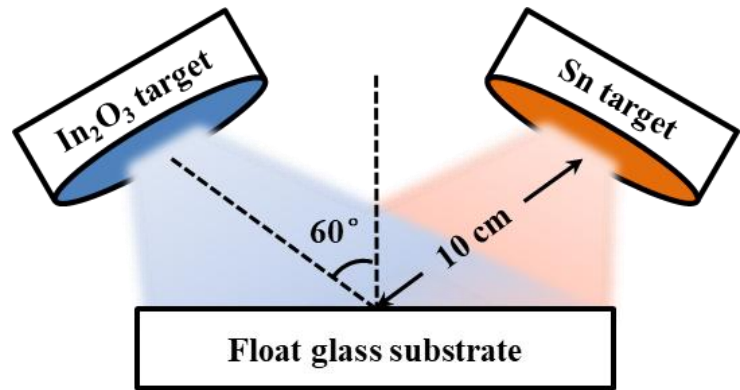
3.3 High-throughput fabrication of ITO multi-component thin films



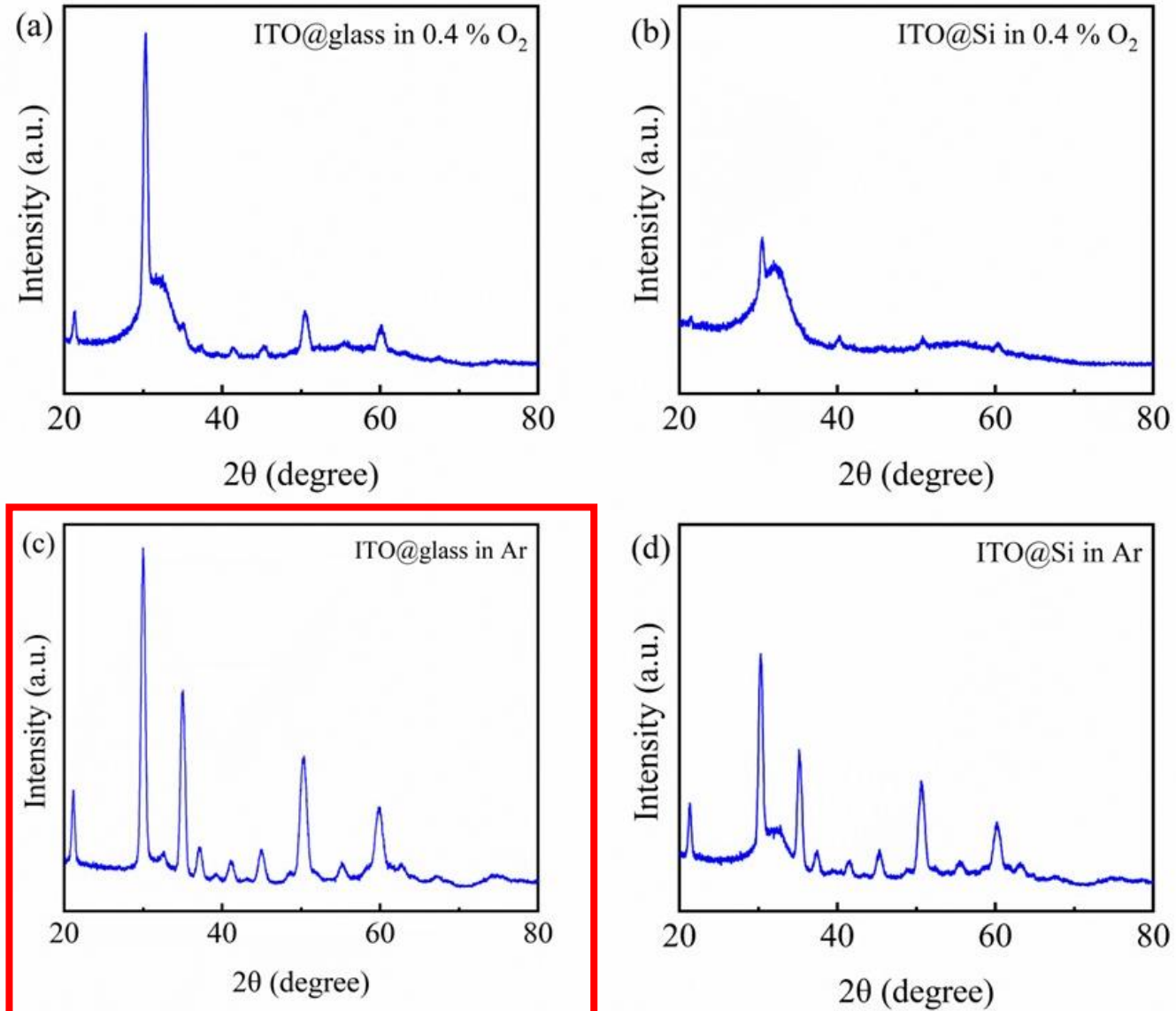
The gradient-component films are **rough** in some areas and have **poor electrical conductivity**.

3.3 High-throughput fabrication of ITO multi-component thin films

Magnetron co-sputtering method by symmetrical targets

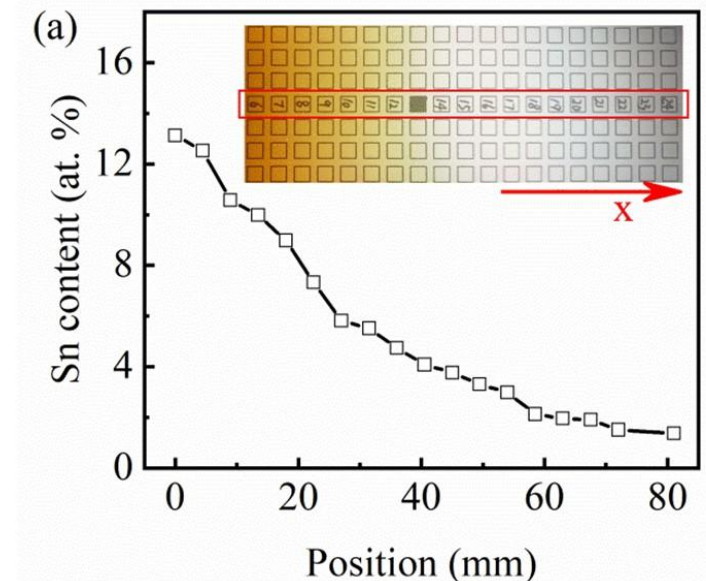
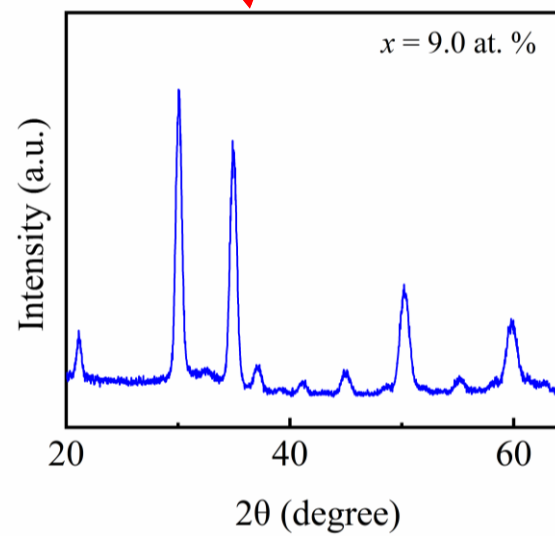
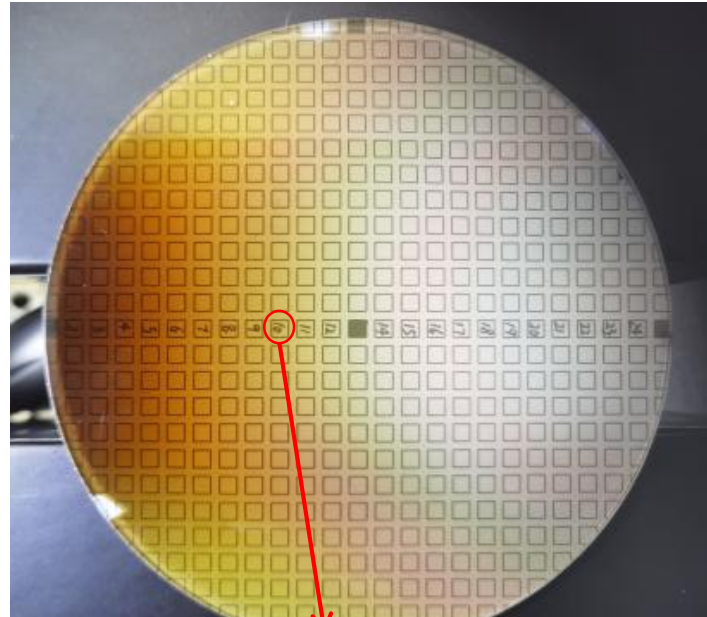


Fixed component deposition In:Sn = 9:1

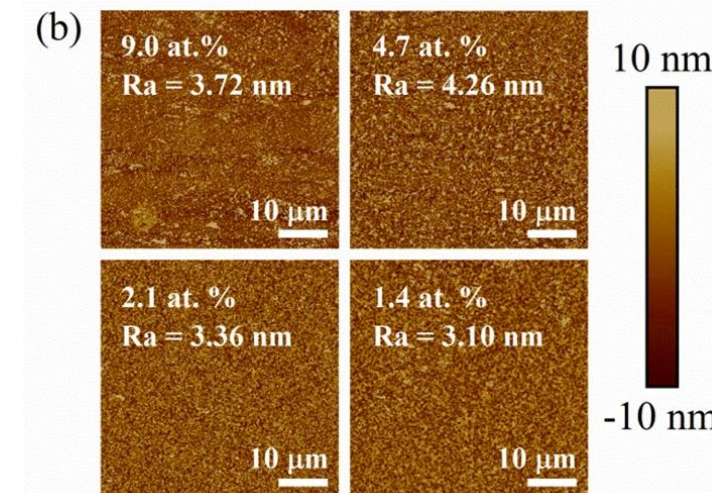




3.4 Gradient components and surface morphology



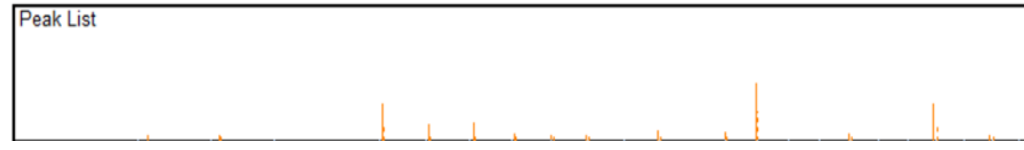
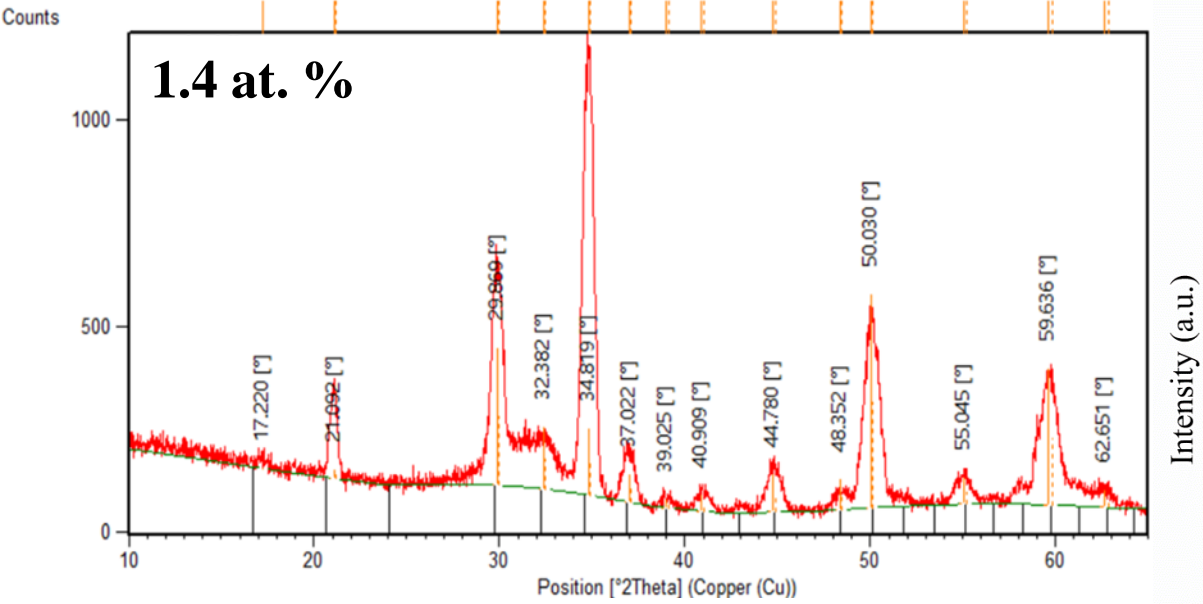
EDS



AFM

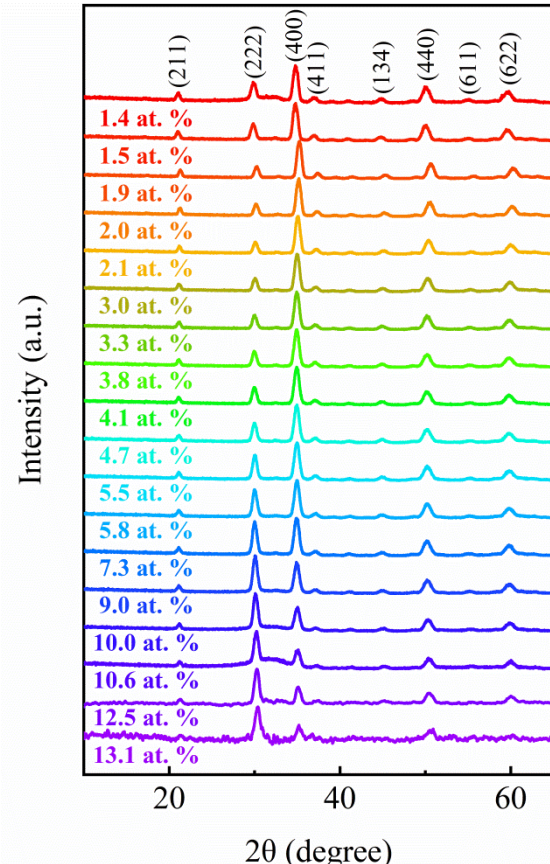
Gradient-component thin film with excellent crystallization and flat surface

3.5 Basic physical property characterization - XRD line scan



#JCPDS 01-089-4598

Characteristic peaks of cubic In_2O_3 unit cells with point group symmetry (Ia-3)



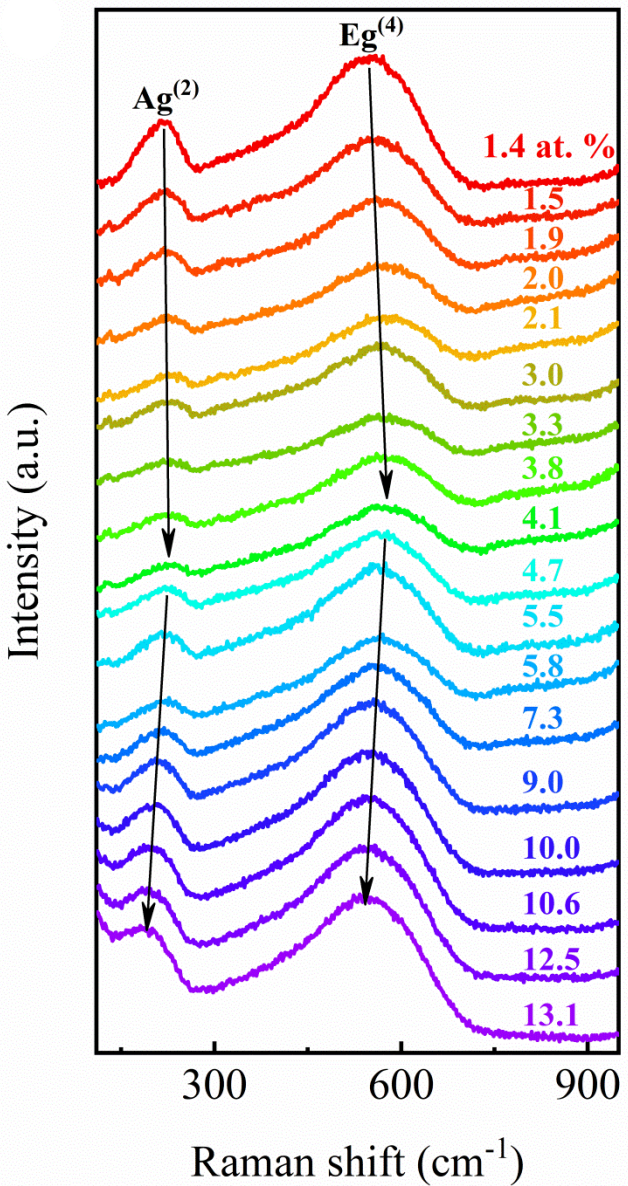
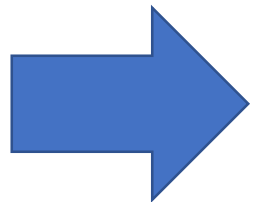
No other phases appear.



The doped Sn atoms did not alter the primitive cells structure.



3.6 Basic physical property characterization - Raman line scan

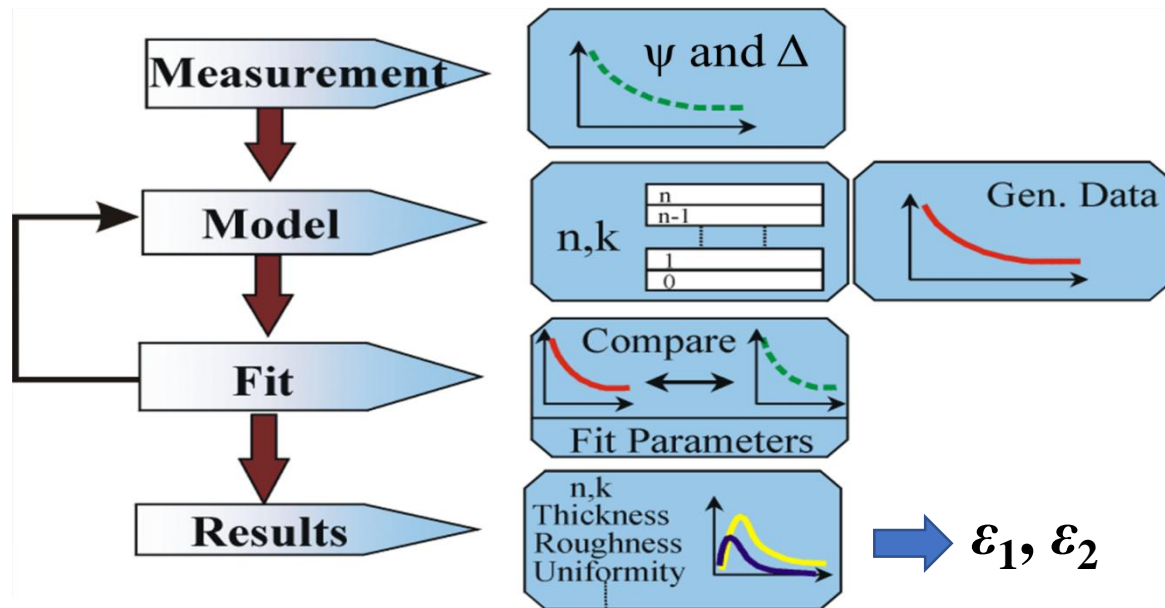
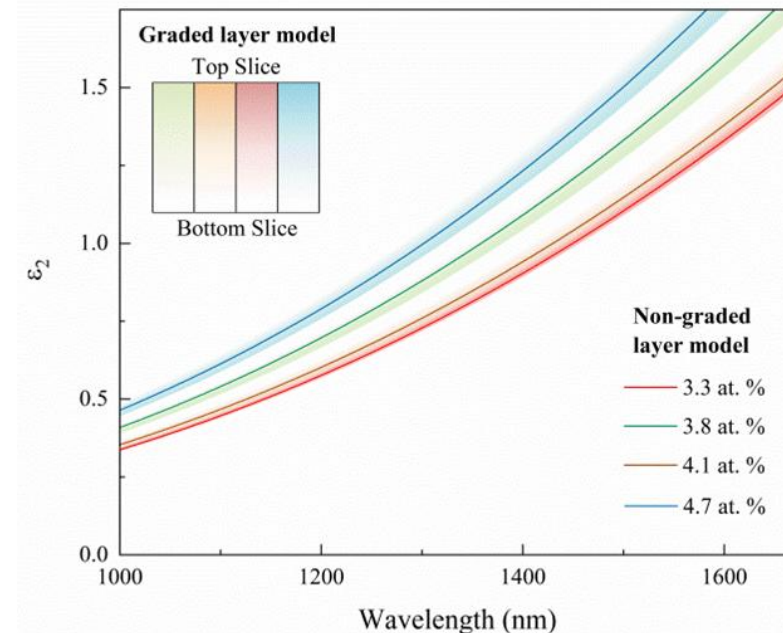
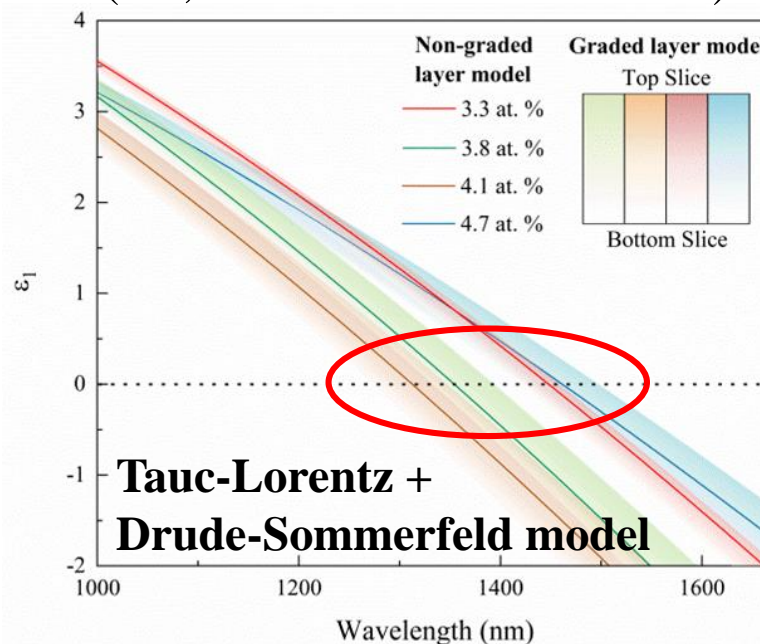




3.7 High-throughput ellipsometric spectra collection

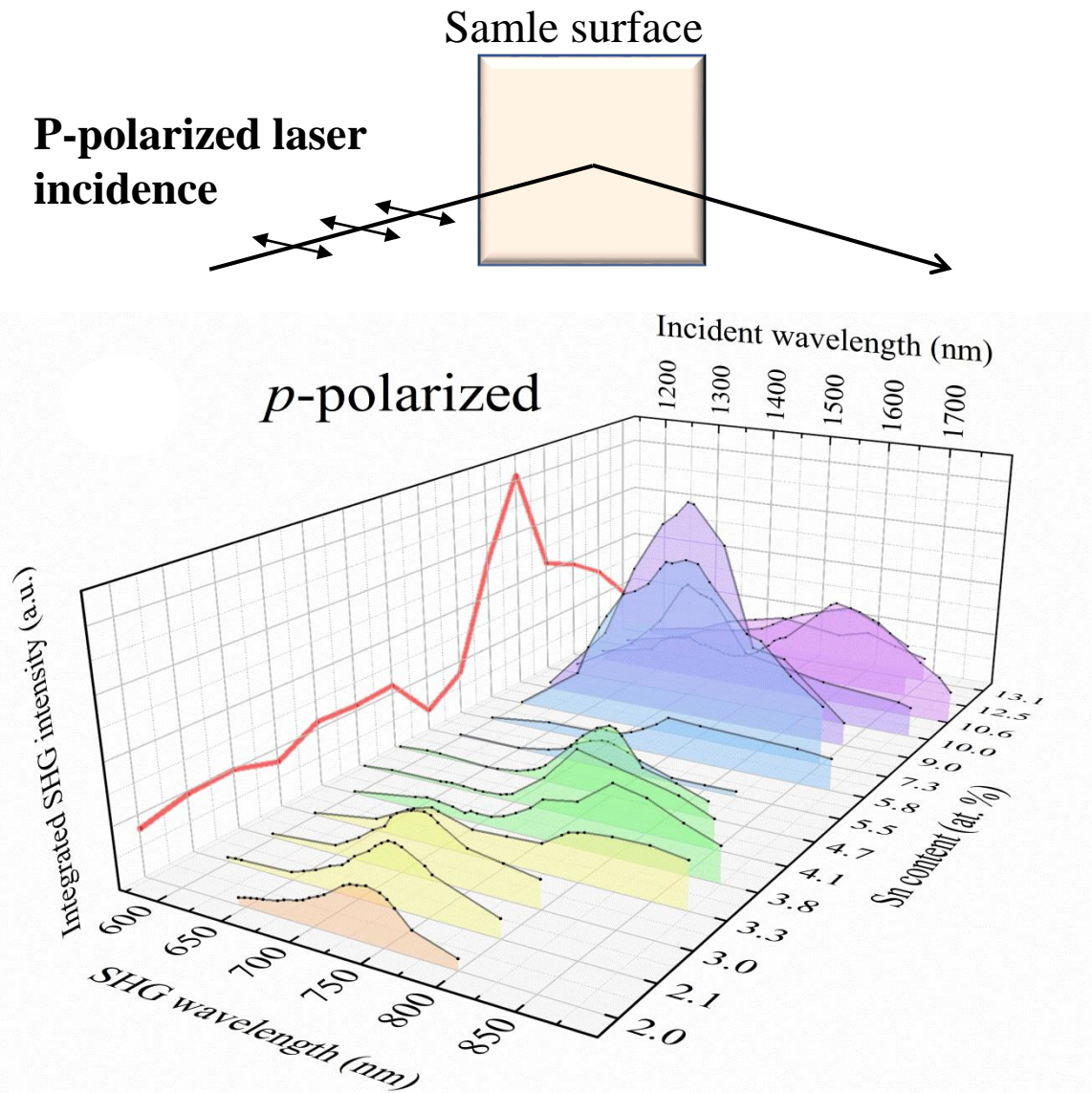
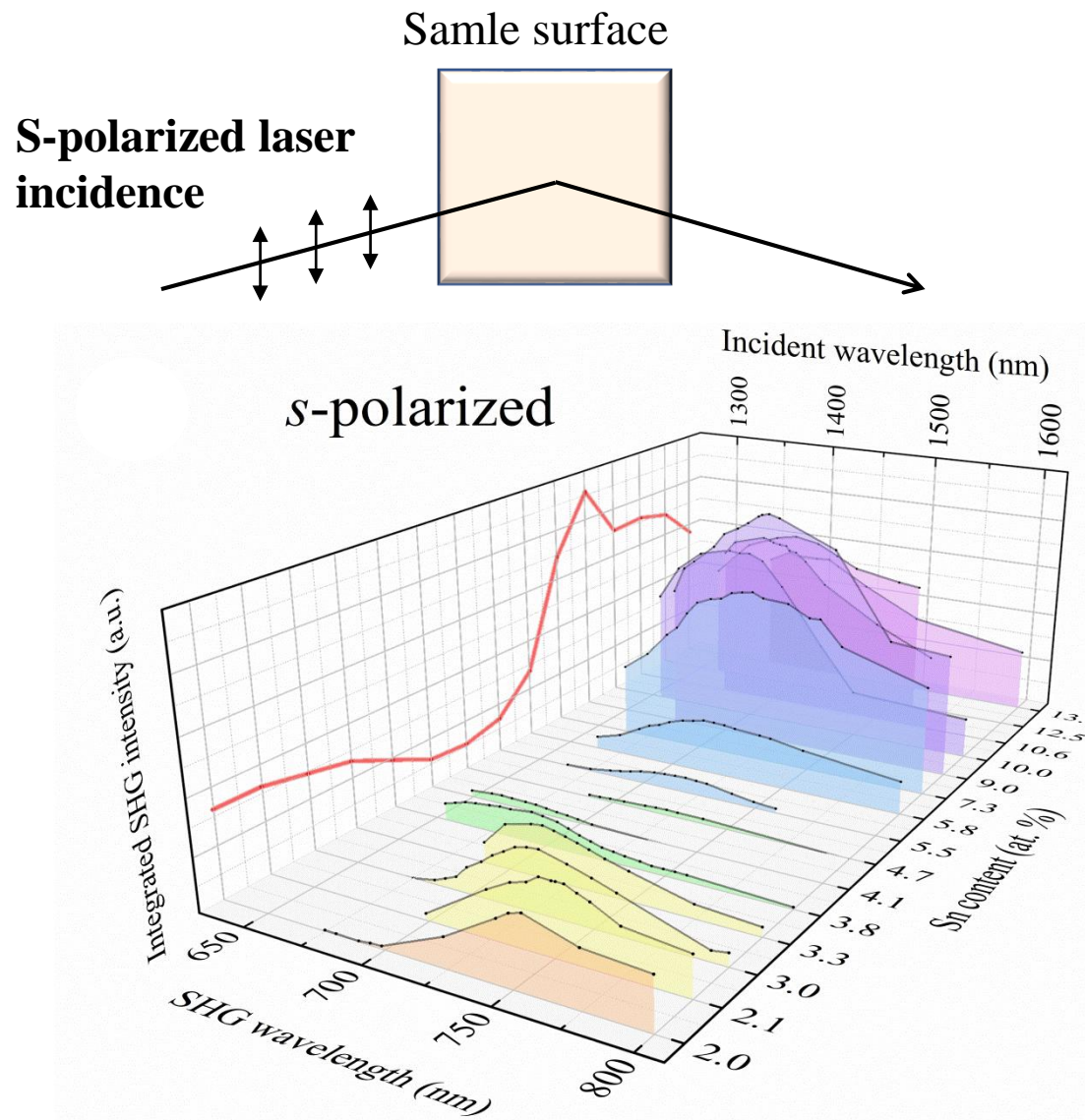


UV-NIR spectroscopic ellipsometry
(SE, J.A.Woollam M-2000X)

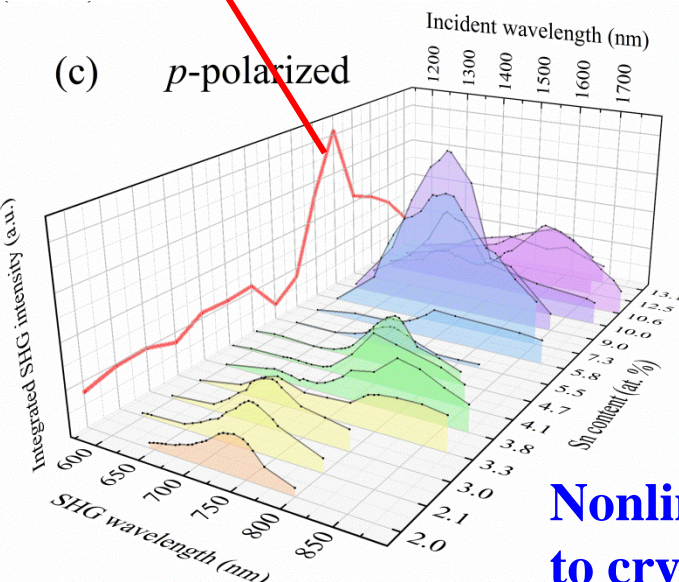
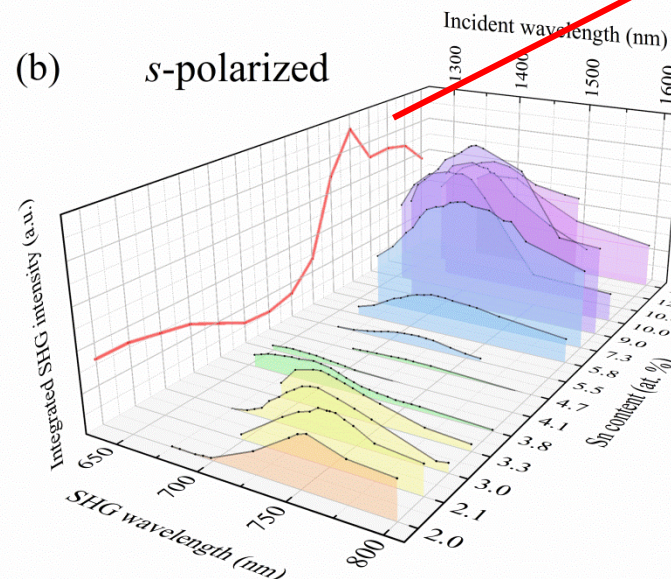
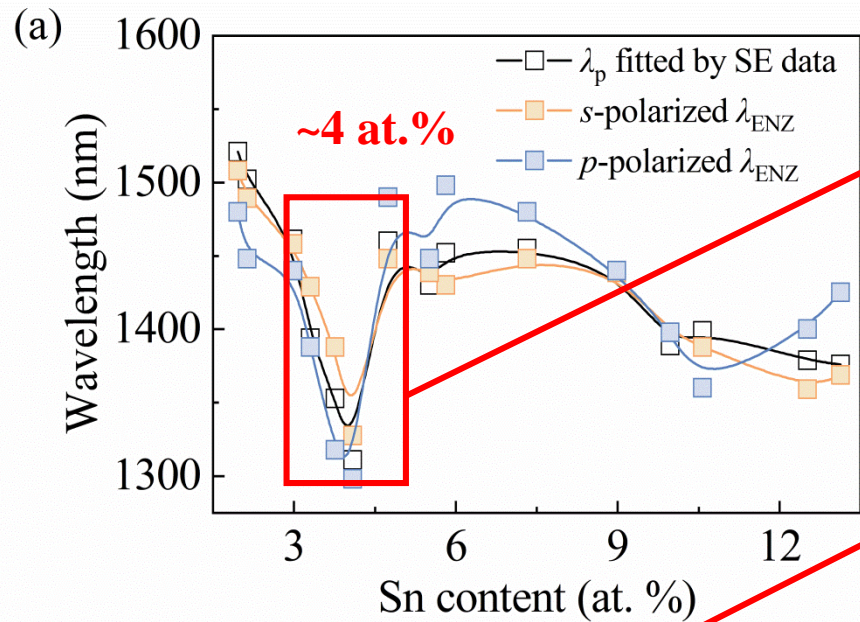


To simplify data analysis
Data fitted by non-graded model was used.

3.8 High-throughput SHG spectra collection



3.9 Physical mechanism linking Sn doping and SHG enhancement of ITO



#1: λ_{ENZ} and λ_p show consistent trend.

#2: When Sn content < 10%, λ_{ENZ} shows non-monotonic behavior

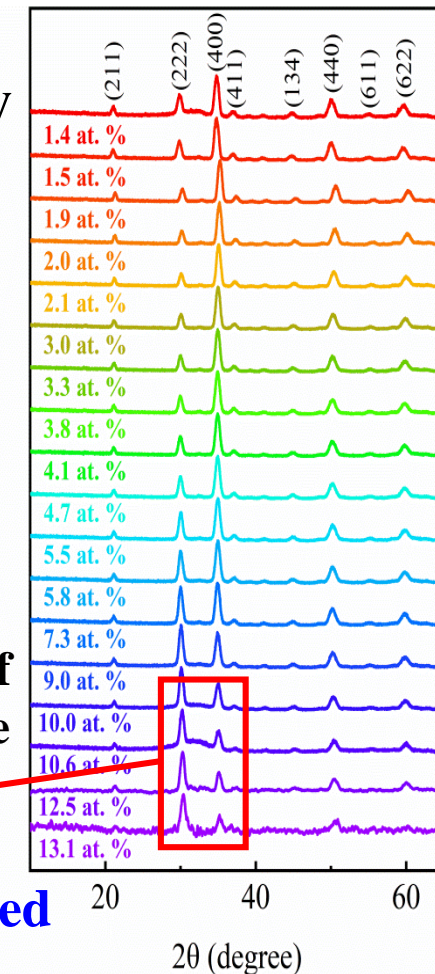
$$\lambda_p^2 = \frac{m^* \epsilon_0 (2\pi c)^2}{N_c e^2}$$

N_c : carrier density

#3: An optimal region of the $(In_{1-x}Sn_x)_2O_3$ film for SHG enhancement is found to be located in the range of 7.3–10.6 at. %.

gradual orientation of the crystal toward the (222) plane

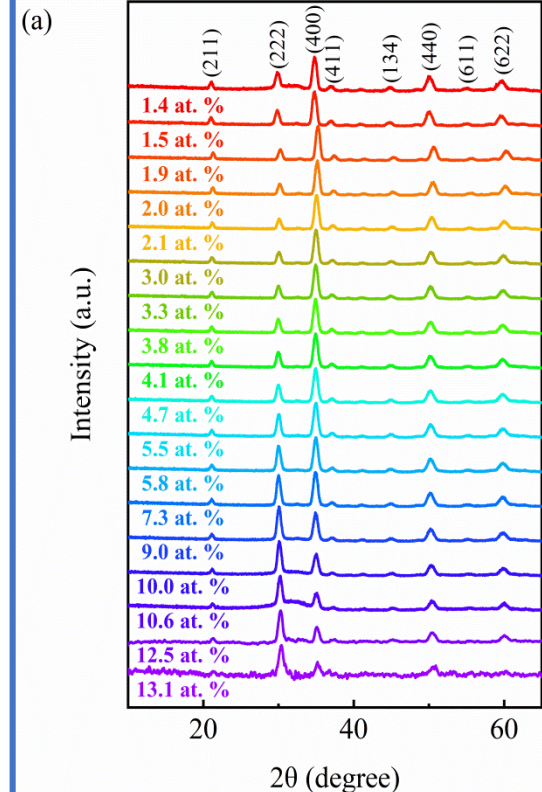
Nonlinear response is related to crystal orientation.



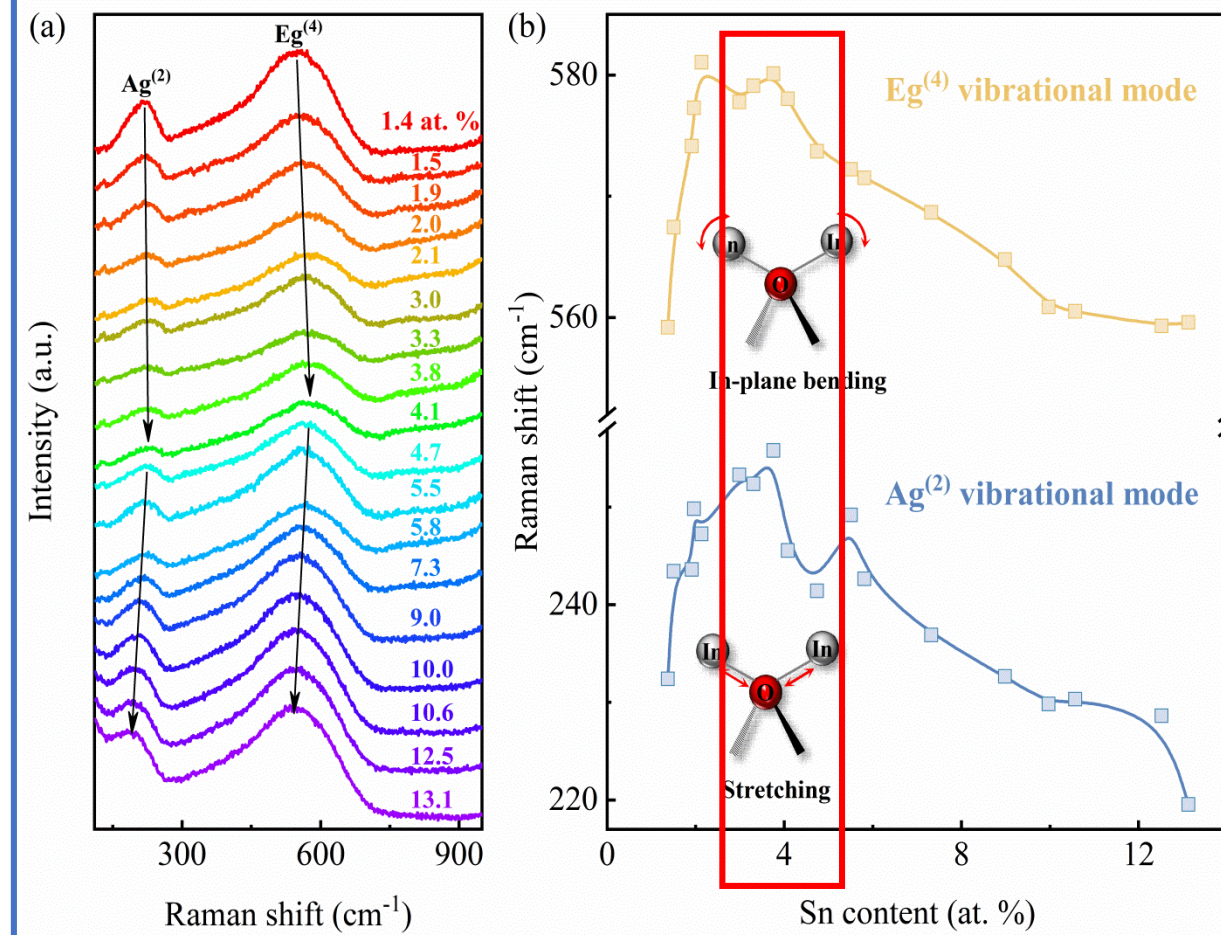


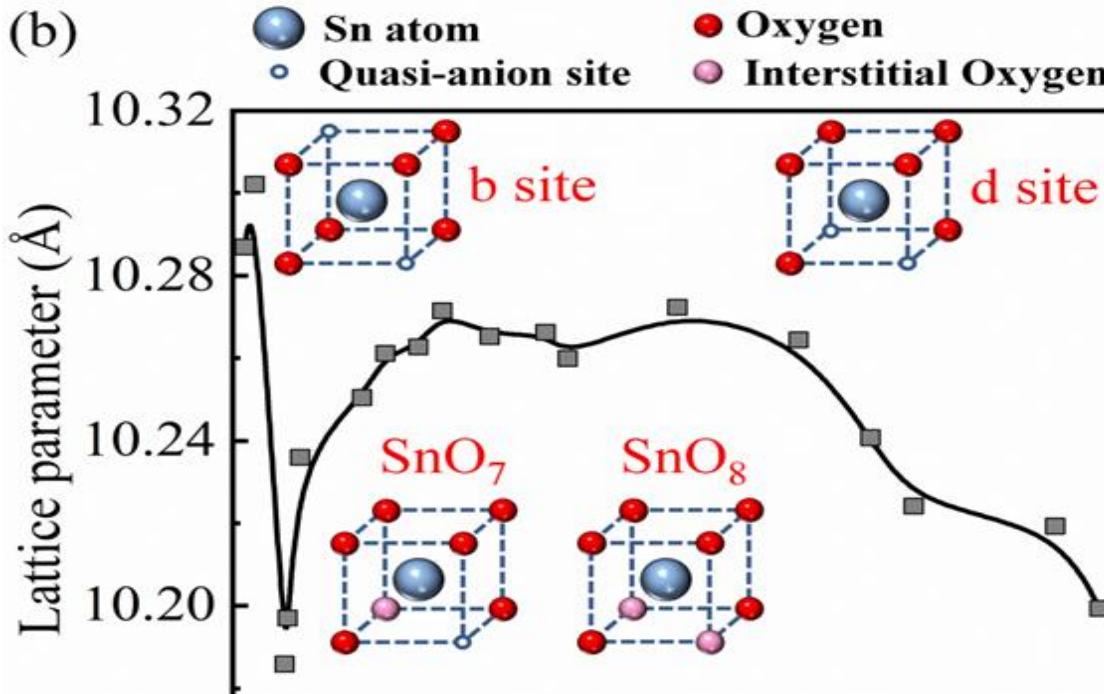
3.10 Mechanism of carrier density effected by different cation positions

XRD



Raman





$X < 4$ at. %

b site

Lattice shrinkage

Blue shift in λ_{ENZ}

$4 \text{ at. \%} < X < 9 \text{ at. \%}$

d site & $\text{SnO}_7, \text{SnO}_8$

Lattice expansion and a gradually stabilized lattice constant

Blue shift and turn to stabilized in λ_{ENZ}

$X > 9$ at. %

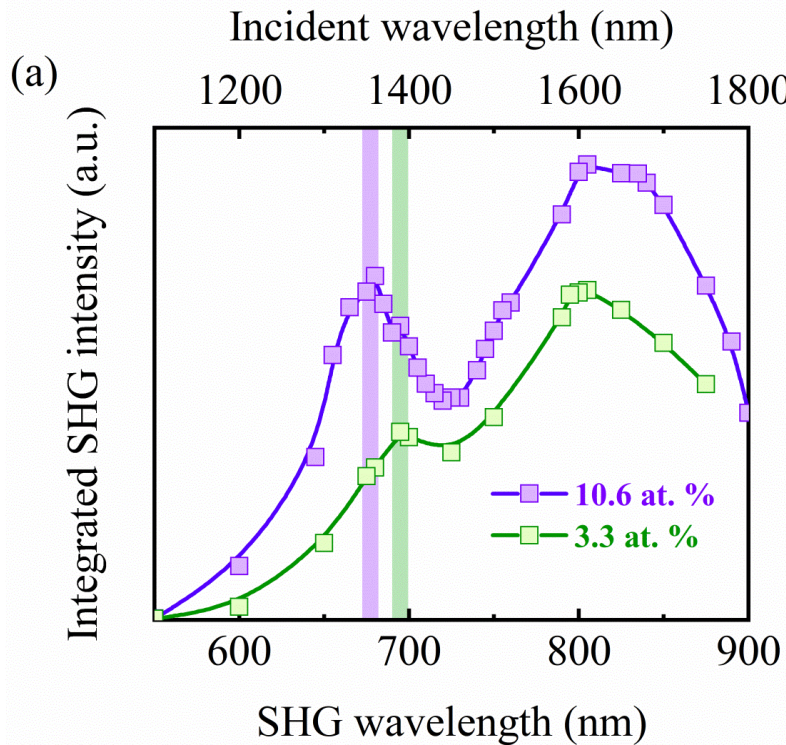
d site

Lattice shrinkage

Blue shift in λ_{ENZ}



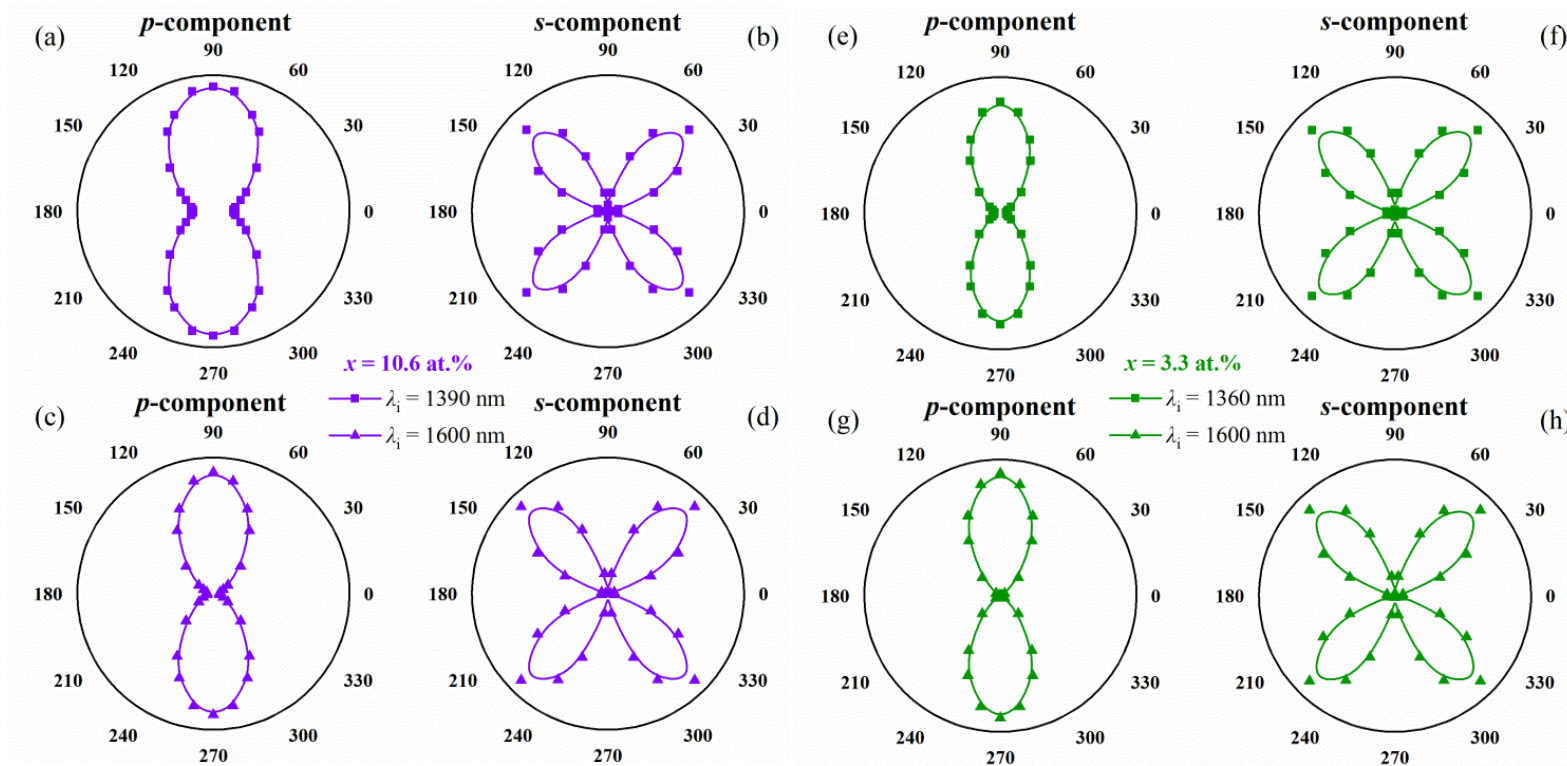
3.11 Anomalous SHG spectra under the p-polarized beam incidence



Hypothesis:

- In-plane isotropy changed?
- The x-component ($E_x^{(\omega)}$) and z-component ($E_z^{(\omega)}$) of the internal electric field peaks were non-overlapping?

$C_{\infty V}$ symmetry group characterization at two representative Sn doping levels (10.6 and 3.3 at. %)

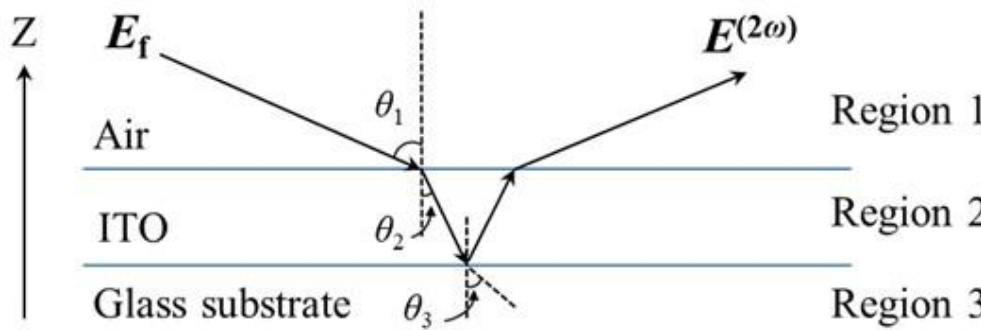


$(In_{1-x}Sn_x)_2O_3$ film with different Sn contents exhibits consistent in-plane isotropy

Rule out the first hypothesis.



3.11 Anomalous SHG spectra under the p-polarized beam incidence



Internal electric field:

$$E_p^{(\omega)} = E_f \cdot T_{12}^{TM} \left[\cos\theta_2 \left(1 - R_{32}^{TM} e^{\frac{4i\pi\cos\theta_2 \cdot D}{\lambda}} \right) \hat{x} + \sin\theta_2 \left(1 + R_{32}^{TM} e^{\frac{4i\pi\cos\theta_2 \cdot D}{\lambda}} \right) \hat{z} \right]$$

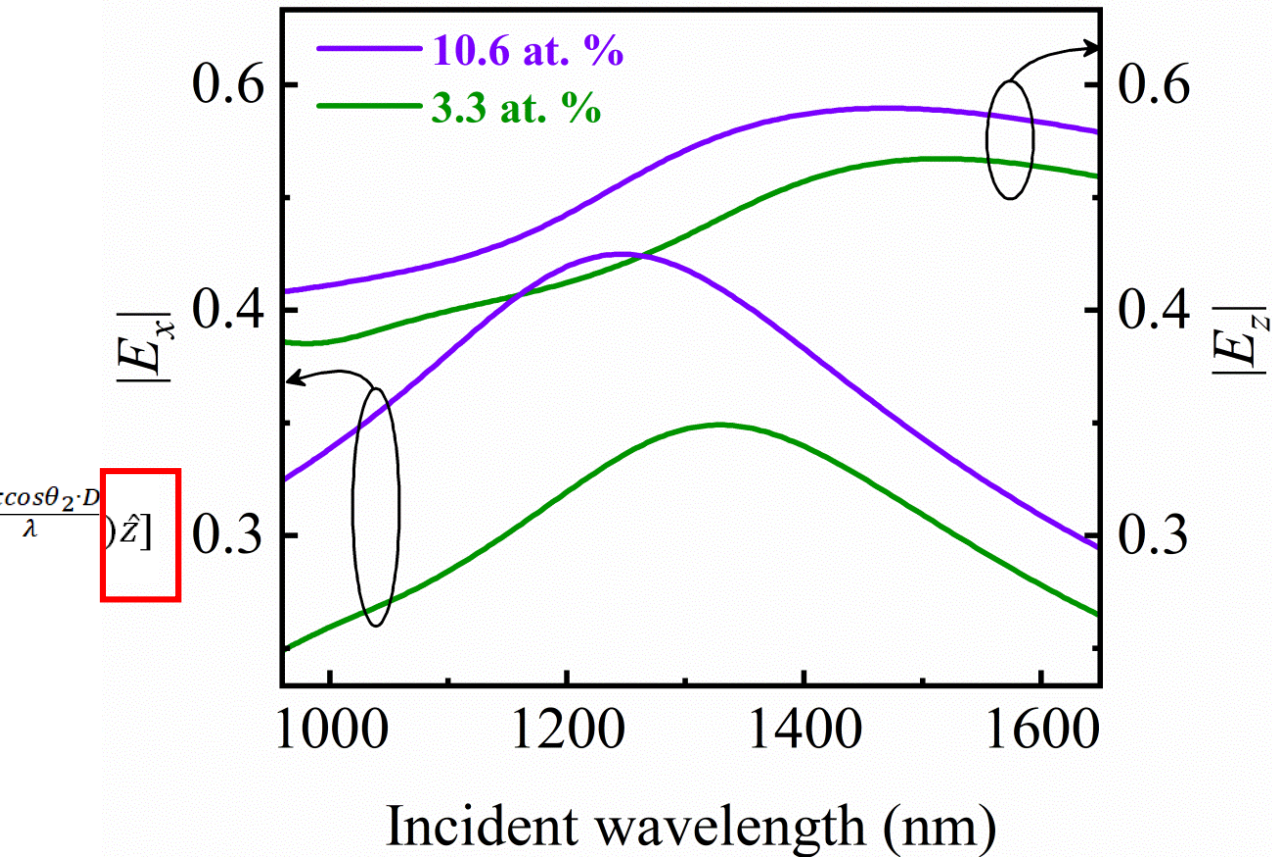
$$E_s^{(\omega)} = E_f \cdot T_{12}^{TE} \cdot \cos\theta_2 \left(1 + R_{32}^{TE} e^{\frac{4i\pi\cos\theta_2 \cdot D}{\lambda}} \right) \hat{y}$$

$$R_{32}^{TM} = \frac{n_3 \cos\theta_2 - n_2 \cos\theta_3}{n_3 \cos\theta_2 + n_2 \cos\theta_3}$$

$$R_{32}^{TE} = \frac{n_2 \cos\theta_2 - n_3 \cos\theta_3}{n_2 \cos\theta_2 + n_3 \cos\theta_3}$$

$$T_{12}^{TM} = \frac{2n_1 \cos\theta_1}{n_2 \cos\theta_1 + n_1 \cos\theta_2}$$

$$T_{12}^{TE} = \frac{2n_1 \cos\theta_1}{n_1 \cos\theta_1 + n_2 \cos\theta_2}$$



$E_x^{(\omega)}$ and $E_z^{(\omega)}$ peaks exhibit distinct non-overlapping and comparable intensities

4 conclusion

System Development:

1. A time-domain micro-area magneto-optical Kerr effect high-throughput characterization system was established, capable of temperature control in the range of 1.7 K–300 K and magnetic field control within ± 7 Tesla. The system achieves a spatial resolution of 36.42 μm and a measurement precision of 0.1%.
2. A high-throughput second-harmonic generation (SHG) characterization system was also constructed, supporting broadband SHG intensity and polarization measurements in the spectral range from 210 nm to 2100 nm.

Film Preparation:

3. Using high-throughput magnetron co-sputtering deposition, gradient-component thin films of $(\text{In}_{1-x}\text{Sn}_x)_2\text{O}_3$ with excellent optical properties were successfully fabricated. The Sn content varied gradually from 1.4 at.% to 13.1 at.%. The films exhibited a smooth surface with a root-mean-square roughness below 10 nm.

4 conclusion

Performance Screening:

4. The most pronounced SHG enhancement effect in $(In_{1-x}Sn_x)_2O_3$ thin films was observed in the Sn composition range of 7.3–10.6 at.%.

Theoretical Innovation:

5. The mechanism of λ_{ENZ} modulation by Sn doping concentration in $(In_{1-x}Sn_x)_2O_3$ thin films was elucidated. According to this physical mechanism, the adjustment of λ_{ENZ} no longer requires complex annealing processes. Instead, it can be conveniently achieved by varying the proportion of Sn substituting at the 24d sites, thereby controlling the concentration of electrically inactive defect clusters.

Wei X, Gu C*, Xiang X-D. Applied Physics Letters, 2023, 123(18): 2201.

Research Experience---Prediction of High-Entropy Alloy Melting Points

09/2021-01/2022

Shenzhen Materials Genome Computing Platform

Project Background: To address the core challenge of sudden performance variations caused by minor compositional changes in the multi-component complex systems of high-entropy alloys, a **data-driven performance prediction model** was constructed. This approach breaks through the bottleneck of the traditional “trial-and-error” method in materials research and development.

Main Work and Achievements:

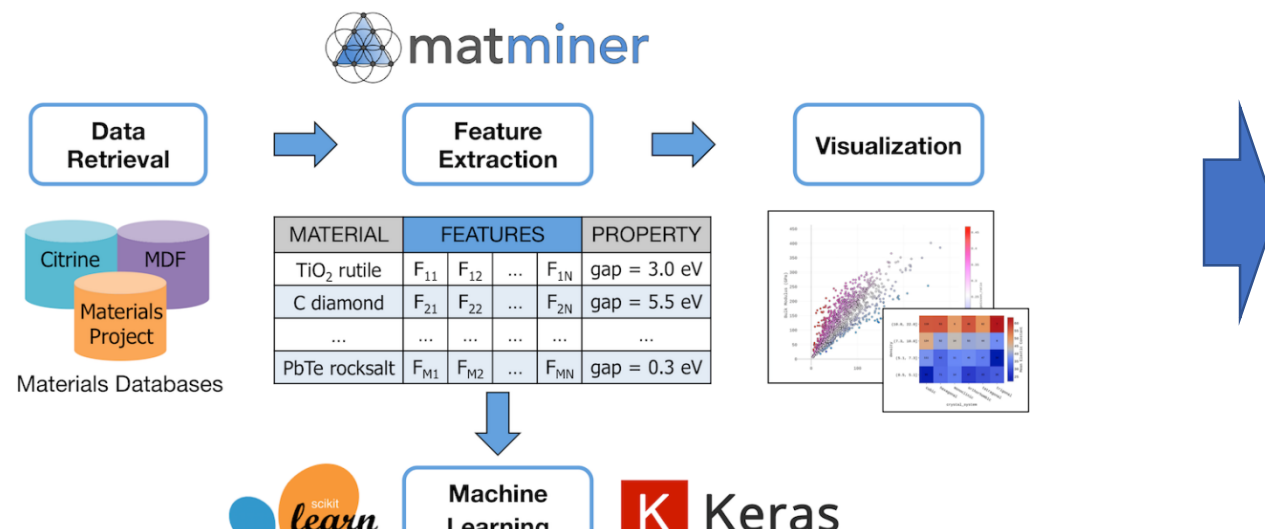
- Self-studied machine learning, Python programming, and Linux server operations.
- Collected and organized theoretical calculation data and experimental data from the literature on alloys, cleaned the dataset, and constructed a high-quality sample set of 1,000 data entries.
- Generated eight feature descriptors, including composition and electronegativity difference.
- Trained an artificial neural network (ANN) prediction model, embedding physical constraints into the output layer.
- Achieved an R^2 value of up to 0.93 on the test set, enabling end-to-end prediction from “composition → property.”

Classification	TensorFlow
Decision tree	sklearn
Logistic regression	PyTorch
...	
Regression	Materials Science Specific
GPR	ænet
KRR	Amp
Multi-linear	Aflow-ML
Random forest	Automatminer
SVR	CGCNN
Neural networks	DeepChem
Graph models	MEGNet
...	PROphet
	SchnetPack
	TensorMol
	...



1 Materials Dataset Construction

- Utilized Matminer to access databases such as Citrine, Materials Project, and MDF, obtaining a wide range of material properties including crystal structures, electronic band structures, and mechanical properties.



- +
- Collected and organized experimental data from the literature for dataset enrichment.

Composition	Rc
Pd95Si5	50000000
Zr66Al8Ni26	66.6
Fe41.5Ni41.5B17	350000
Zr65Be35	10000000
Mg65Cu20Y10Zn5	25
Zr55Al19Co19Cu7	16
Zr41.2Ti13.8Cu12.5Ni10Be22.5	1.4



2 Feature Generation

Elemental Property Features:

Element Properties		
Number	Valence Electrons	Unfilled Valence Electrons
Mendeleev Number	s Valence Electrons	Unfilled s Valence Electrons
Atomic Weight	p Valence Electrons	Unfilled p Valence Electrons
Column	d Valence Electrons	Unfilled d Valence Electrons
Row	f Valence Electrons	Unfilled f Valence Electrons
Covalent Radius	Melting Point	Volume Per Atom
Electronegativity	Magnetic Moment	Space Group Number
Band Gap		

Ward, L. et al. *npj Comput Mater* **2**, 1–7 (2016).

Elemental Statistical Features

min	$\text{Min}(\{p_i\})$
max	$\text{Max}(\{p_i\})$
range	$\text{Max}(\{p_i\}) - \text{Min}(\{p_i\})$
mean	$\bar{p}_i = \sum x_i p_i$
avg_dev	$\sum x_i p_i - \bar{p}_i $
mode	$p_i (i = \text{argmax } x_i)$

Valence Electron Occupancy

$$F_m = \frac{\sum x_i n_e^m}{\sum x_i n_e} \quad (m = s, p, d, f)$$

p_i : elemental properties x_i : composition ratio

n_e^m : the number of valence electrons in m orbital n_e : total valence electron count



3 Feature Selection

Three-Step Filtering Method

Variance
Filtering

- Remove features with variance lower than 0.1.

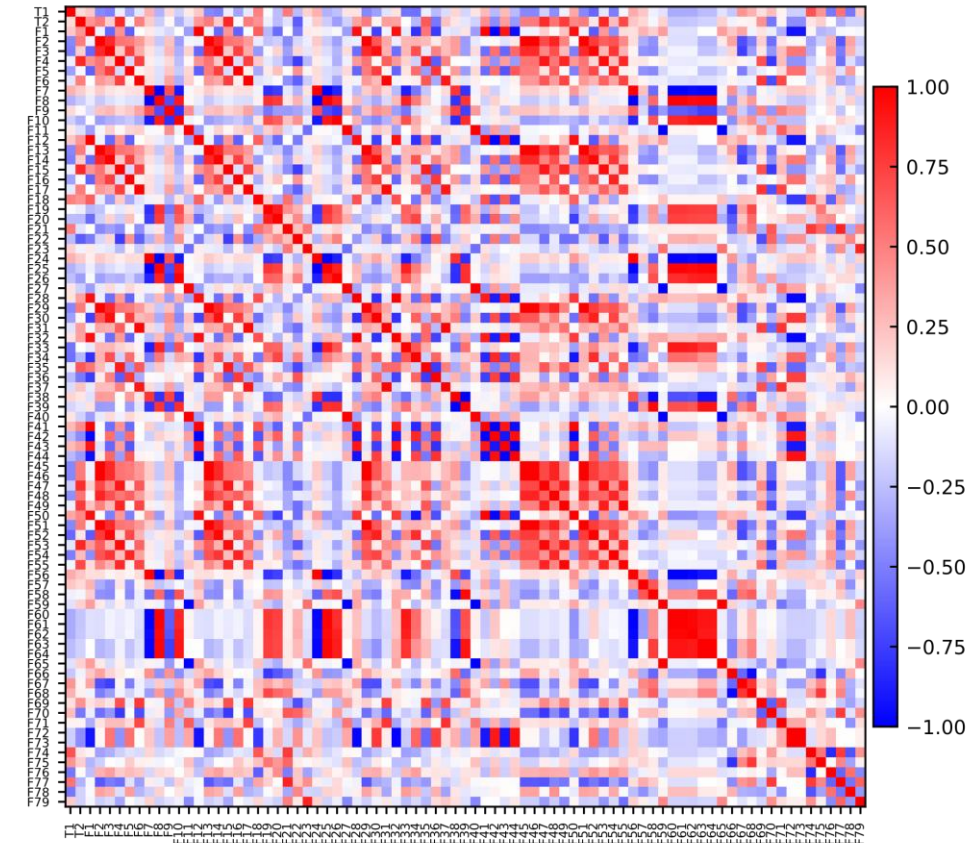
PCC

- Based on the Pearson correlation coefficient (PCC), eliminate redundant features from highly correlated feature pairs and discard features with weak correlation to the target property.

RFE

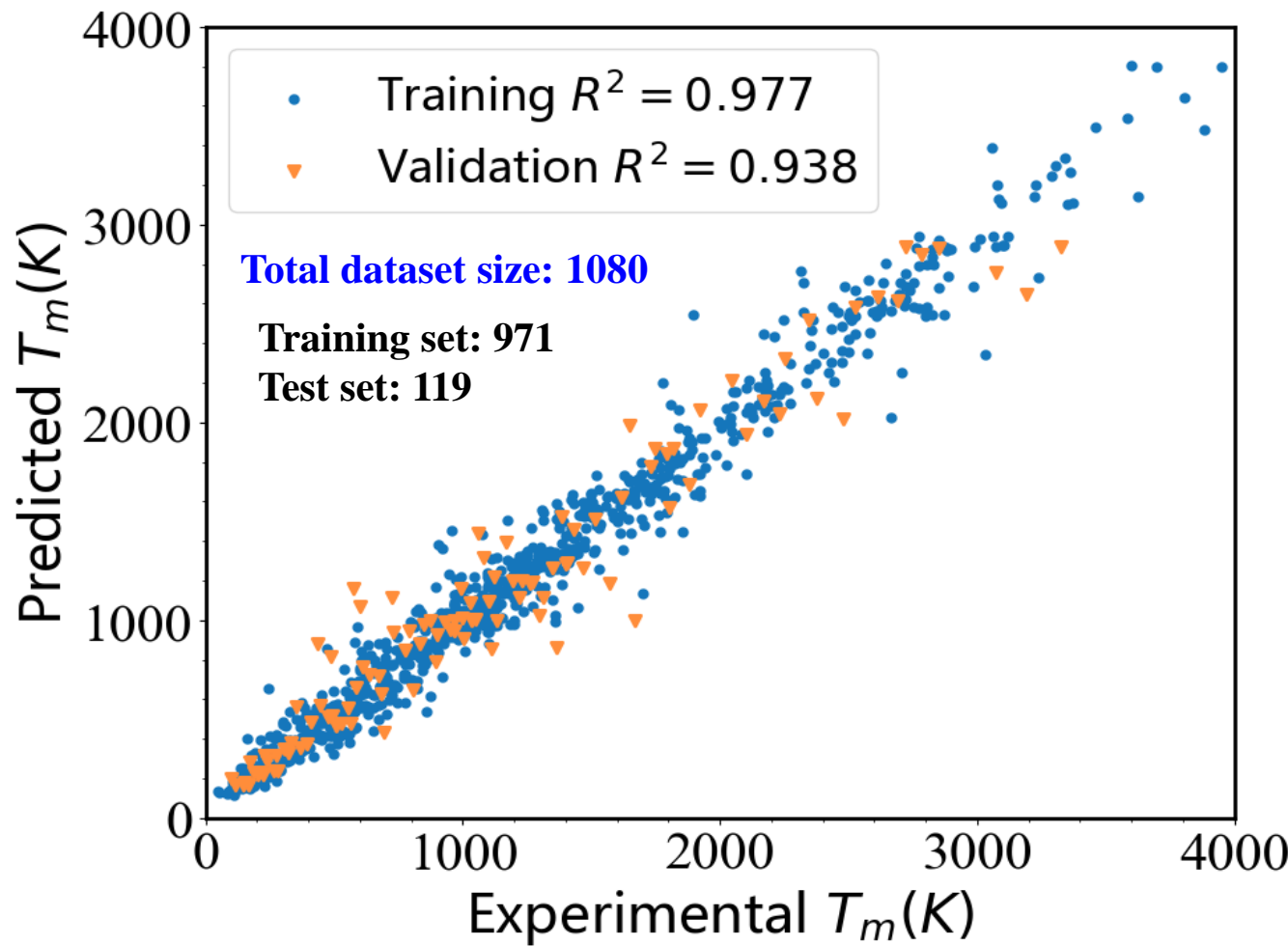
- Apply Recursive Feature Elimination (RFE) to iteratively remove unimportant features and obtain the optimal feature subset until convergence.

PCC Matrix





4 Model Training and Validation



Prediction results obtained for GST materials

